Analysis of translating mitoribosome reveals functional characteristics of protein synthesis in mitochondria of fungi

Yuzuru Itoh[1,2†], Andreas Naschberger[1†], Narges Mortezaei[1†], Johannes Herrmann[3] and A. Amunts[1,2*]

[1]Science for Life Laboratory, Department of Biochemistry and Biophysics, Stockholm University, 17165 Solna, Sweden

[2]Department of Medical Biochemistry and Biophysics, Karolinska Institutet, 17165 Solna, Sweden

[3]Cell Biology, University of Kaiserslautern, Erwin-Schrödinger-Straße 13, 67663 Kaiserslautern, Germany

† These authors contributed equally to this work.

* email: amunts@scilifelab.se

Abstract

Mitoribosomes have been specialized for protein synthesis in mitochondria. While it is established that mitoribosomes differ between species, a reference model from the Fungi kingdom is missing, and the structural basis for the mitoribosomal function is not understood. We report models of the translating fungal mitoribosome with mRNA, tRNA and nascent polypeptide, as well as an assembly intermediate, determined from cryo-EM maps at overall resolution of 2.98-3.09 Å. Most of the rRNA expansion segments were modeled, and five additional associated proteins were identified. Mitochondria-specific mS27 is found to have a function of linking two expansion segments. Collectively, the expanded rRNA and mitochondria-specific protein elements coordinate binding of nicotinamide adenine dinucleotide (NAD) in the central protuberance of the large subunit and the ATPase inhibitory factor 1 (IF_1) in the small subunit, revealing unprecedented occurrences in translation apparatus. The models of the active fungal mitoribosome explain how mRNA binds through a dedicated protein platform on the small subunit, tRNA translocated with the help of newly identified protein mL108 bridging it with L1 stalk on the large subunit, and nascent polypeptide paths through the exit tunnel involving a series of conformational rearrangements. Finally, an assembly intermediate is found and modeled with the maturation factor Atp25, providing insight into the biogenesis of the mitoribosomal large subunit and translation regulation.

Proteins synthesis in mitochondria supports bioenergetics of eukaryotic cells and executed by dedicated mitoribosomes. Cryo-EM has been instrumental in revealing the first structural snapshots of mitoribosomes. While for mammals the obtained models from human embryonic kidney cells (Brown, Amunts et al. 2014, Amunts, Brown et al. 2015) are in agreement with those from porcine and bovine tissues (Greber, Boehringer et al. 2014, Greber, Bieri et al. 2015), the structure of the mitoribosome from the yeast *Saccharomyces cerevisiae* displayed considerable specializations (Amunts, Brown et al. 2014, Desai, Brown et al. 2017, Petrov, Wood et al. 2019). Particularly, it proposed a distinct composition and putative deviations in the functionally defining features of translation, including an expanded mRNA channel exit and rerouted polypeptide exit channel. Although the cryo-EM data is informative, the deviations of the mitoribosome from a single-celled, complex I lacking, *S. cerevisiae* cannot be considered as a prototypic example, but more likely species-specific. In addition, the available models are incomplete due to the limited resolution. Functionally, since the models were derived from dormant mitoribosomes, without tRNA bound to mRNA and nascent polypeptide, the mechanism of action and roles of specific proteins could not be understood. Therefore, in the absence of high-resolution structural information of translating mitoribosome, key questions regarding mitochondrial translation remain open. To provide a representative reference for studying protein synthesis in the mitochondria of fungi, and to reveal how the mitoribosome functions in coordination with its translation partners, we determined structures of the translating mitoribosome from the representative fungal model organism *Neurospora crassa.*

Model organism

N. crassa has been recognized as the organism used for answering a variety of fundamental biological questions (McCluskey and Baker 2017), including the seminal demonstration of the one-gene, one-enzyme hypothesis (Beadle and Tatum 1941), construction of a densely populated genetic map (David D. Perkins 1962), and cytogentic markers (Perkins, Radford et al. 2001). Being an established model organism, it was also the first among the filamentous fungi, which genome was sequenced of (Galagan, Calvo et al. 2003). Since then *N. crassa* serves as a model organism for the areas of cell biology and physiology, including analysis of the endogenous circadian rhythm (Baker, Loros et al. 2012) that is tightly associated with the mitochondrial activity (de Goede, Wefers et al. 2018). Specifically in the field of the mitochondrial translation, the pioneering research that has established the field was performed with *N. crassa*. This includes early characterization of the physicochemical properties of the mitoribosomes and the base composition of its mt-rRNA (Kuntzel and Noll 1967), the finding that mitoribosomal intactness requires a relatively high magnesium concentration (Kuntzel 1969), studies showing radioactive amino acid incorporation into mitoribosome (Neupert, Sebald et al, 1969), the finding that Oxa1 facilitates integration of mitochondrially encoded proteins into the inner membrane (Nargang, Preuss et al. 2002), and the first evolutionary analysis of the mitoribosome (van der Sluis, Bauerschmitt et al. 2015). Following these considerations, to provide a reference for the process

of protein synthesis in mitochondria, we set to investigate the translating mitoribosome from the model organism filamentous fungus *N. crassa.*

Structure determination

In order to characterize a representative functional mitoribosome, the *N. crassa* mycelia of the strain K5-15-23-1 overexpressing the protein Oxa1 (Nargang, Preuss et al. 2002) were grown aerobically, and translation was stalled using chloramphenicol prior to harvesting. The mycelium was dried, lysed with mortar and pestle, and the mitoribosomes were purified as described previously (Aibara, Andréll et al. 2018), and subjected to cryo-EM analysis. The cryo-EM consensus map was obtained from 131,806 particles at overall resolution of 2.86 Å (Supplementary Fig. 1), representing a considerable improvement of the published data from *S. cerevisiae*. Because of the relative movement between the large subunit (mtLSU) and the small subunit (mtSSU), the models were built from independently masked refined consensus maps (Supplementary Table 1,2).

The 3D classification resulted in two reconstructions of the mitoribosome corresponding to the ratcheted and non-ratcheted states (Supplementary Fig. 1). After subtracting the mitoribosome signals outside the tRNA binding sites, followed by focus 3D classifications, we obtained three distinct classes of mitoribosome with a tRNA occupying P-site (P/P), E-site (E/E), and in the hybrid P/E state, at the overall resolutions of 3.05, 3.09, and 2.98 Å, respectively (Supplementary Fig. 1). In the P/P and P/E tRNA states, we detected and modeled co-purified native mitochondrial mRNA, and the density corresponding to the nascent polypeptide was identified.

To further improve the local resolution, focused masked refinements were performed using the masks for the mtLSU core, central protuberance (CP), L1 stalk, L10m region, mtSSU head, body and tail (Supplementary Fig. 1). Consequently, the resolutions were improved to ~2.50-3.40 Å throughout most of the regions. The quality of the maps allowed building the most complete available model, including identification of five proteins previously missed: uL1m, uL10m, uL11m, mL53 and mL54; two newly identified mitoribosomal proteins: mL108 and the ATP synthase inhibitory factor 1 (IF_1); and 60 proteins with some higher completeness, as well as the rRNAs.

We noted that mitoribosomes from actively growing *N. crassa* mycelia contain a pool of free mtLSU, which resembles the profile obtained from the mitochondria of human embryonic kidney cells (Brown et al. 2017). Unlike the mtLSU in the intact mitoribosome, this population missing the density for bL9m, but has an extra factor Atp25 bound to uL14m, and a poor density at the interface consistent with unfolded mt-rRNA. The quality of the structural data allowed analyzing the differences with the mature mtLSU, and propose putative regulatory mechanism.

Overall structure and new features

The fungal mitoribosome consists of 78 different proteins (Fig. 1, Table S2-S3), 23S and 16S rRNAs. The proteins mS42 and IF_1 are found in two copies as homodimers. 48 bacterial orthologs are extended, and 30 proteins are mitochondria specific (Supplementary Fig. 2). For the

rRNA, we modeled 16 expansion segments (ES), 15 of which are in the mtLSU (Supplementary Figs. 3 and 4), and several other rRNA regions have been reduced. The deletion in the mtDNA genome are not correlated with a specific functional feature or attributed to selective loss/gain of activity, but rather reflect a general reductive phase in the mitochondrial genome (van der Sluis, Bauerschmitt et al. 2015). For the native mitochondrial tRNAs (P/P, P/E, E/E states) and mRNA, we modeled sequences that fit the corresponding densities the best, because those densities represent a mixture of different tRNAs and mRNAs in mitochondria.

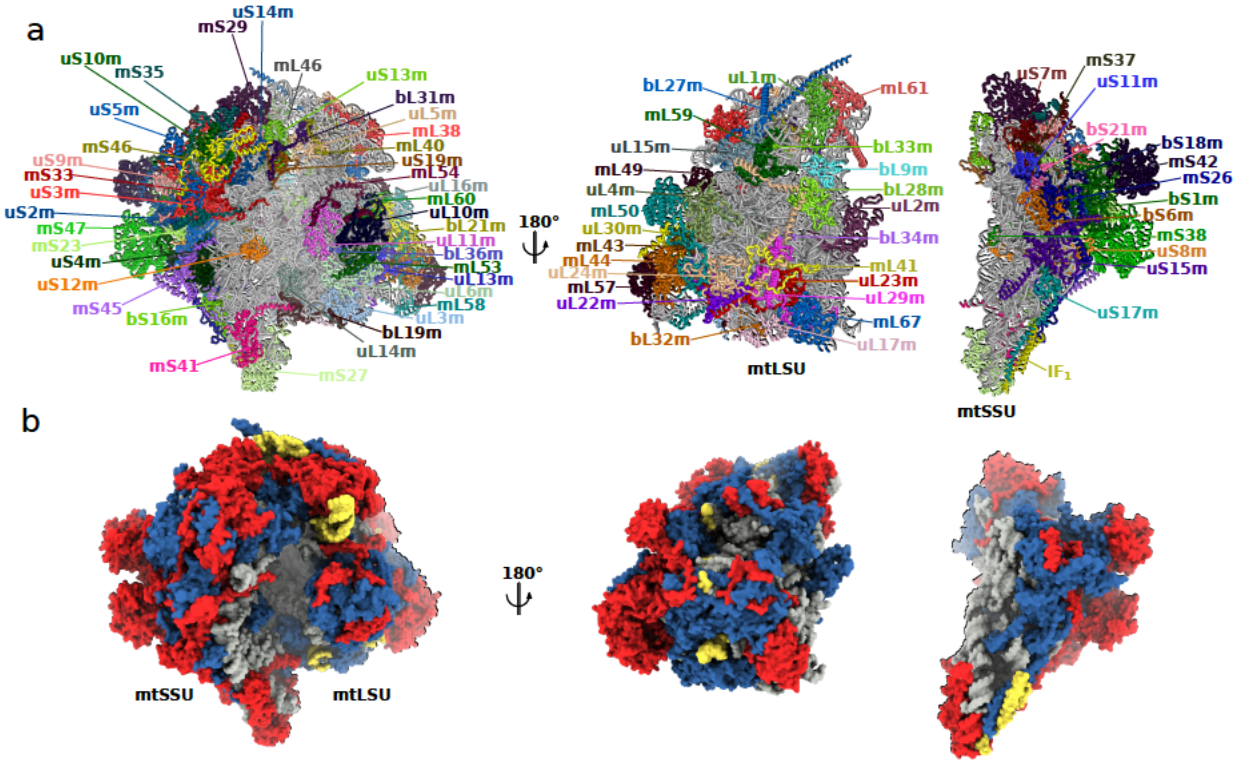

Figure 1: Structure of the fungal mitoribosome. a, Overall structure of the complete mitoribosome and its subunits with indicated mitoribosomal proteins.

Some of the improvements in the model due to the high-resolution map are exemplified in Figures 1 and 2. We identified protein mS27 directly from the density in the region, and it occupies the positions of the previously mis-assigned protein mS44 and '*unknown α-helical protein B*' (Fig. 2a, Supplementary Fig. 5). Another example is the protein mS29 that was reported as a GTPase involved in apoptosis, and mutations in the P-loop motif of the nucleotide binding pocket were suggested to impair this function (Kim, Maiti et al. 2017). In the nucleotide pocket of mS29, which was previously modeled with guanosine diphosphate (GDP), we can see at the local resolution of 2.77 Å that the density for N2 purine ring atom is missing, and the correct assignment for the nucleotide is adenosine triphosphate (ATP) (Fig. 2e, Supplementary Fig. 6). This is further supported by the better resolved chemical environment formed by Leu150

136 of mS29, which would be incompatible with guanine since the O6 carbonyl of guanine imparts
137 repulsive interaction with the backbone carbonyl of Leu150 (acceptor with acceptor), and the
138 NH1 group of guanine forms a second repulsive interaction with the backbone NH group of
139 Leu150 (donor with donor). Placing an ATP instead of GDP leads to a more favorable mode of
140 interactions in this region.

141 At the CP, we found NAD in the binding pocket formed by mL40, uL5m, and rRNA H84-ES3
142 (Fig. 2b). Positively charged residues of mL40 and uL5m interact with the negatively charged
143 NAD phosphates. The pyridine ring of the nicotinamide is held in place by π-stacking on the base
144 pair of A2755 and U2759. Arg295 of mL40 forms π-stacking at the other side of the NAD
145 pyridine. Therefore, NAD bridges the mitoribosomal proteins and the mt-rRNA at the core of CP.
146 This implies regulatory function in the assembly of the mtLSU based on the local NAD level.

147 The natural inhibitor of the mitochondrial ATP synthase IF_1 is bound to the mtSSU tail as a
148 homodimer, which is its active state (Fig. 2c). IF_1 inhibits the ATP synthase activity by inserting
149 its N-terminal part into the catalytically active F_1 domain, thereby blocking its rotational
150 movement and subsequently its hydrolase and synthase activities (Esparza-Molto, Nuevo-
151 Tapioles et al. 2017). The mtSSU-bound IF_1 was identified directly from the density, due to the
152 characteristic coiled-coil homodimerization of the C-terminal helix and side-chain fitting. It binds
153 to the rRNA h44, mS27, and the C-terminal extension of uS17m that forms a helical bundle with
154 the coiled-coil (Supplementary Fig. 7). A metal ion Mg^{2+} bridges a backbone phosphate of h44
155 with side chains of uS17m and IF_1. The topology of IF_1 is such that N- and C-termini of each
156 monomer point in the opposite direction: one towards the mtSSU body, and the other towards the
157 solvent. The latter appears to have a similar conformation to the canonical binding on the ATP
158 synthase. The mtSSU rRNA h44 is expanded and coordinated by uS17m extension, which
159 suggests that IF_1 has been acquired through the mechanism of 'structural patching' to stabilize
160 the rapidly evolving growth (Petrov, Wood et al. 2019). Functionally, IF_1 may link the biogenesis
161 of mitoribosome to the ATP synthesis assembly and inhibition.

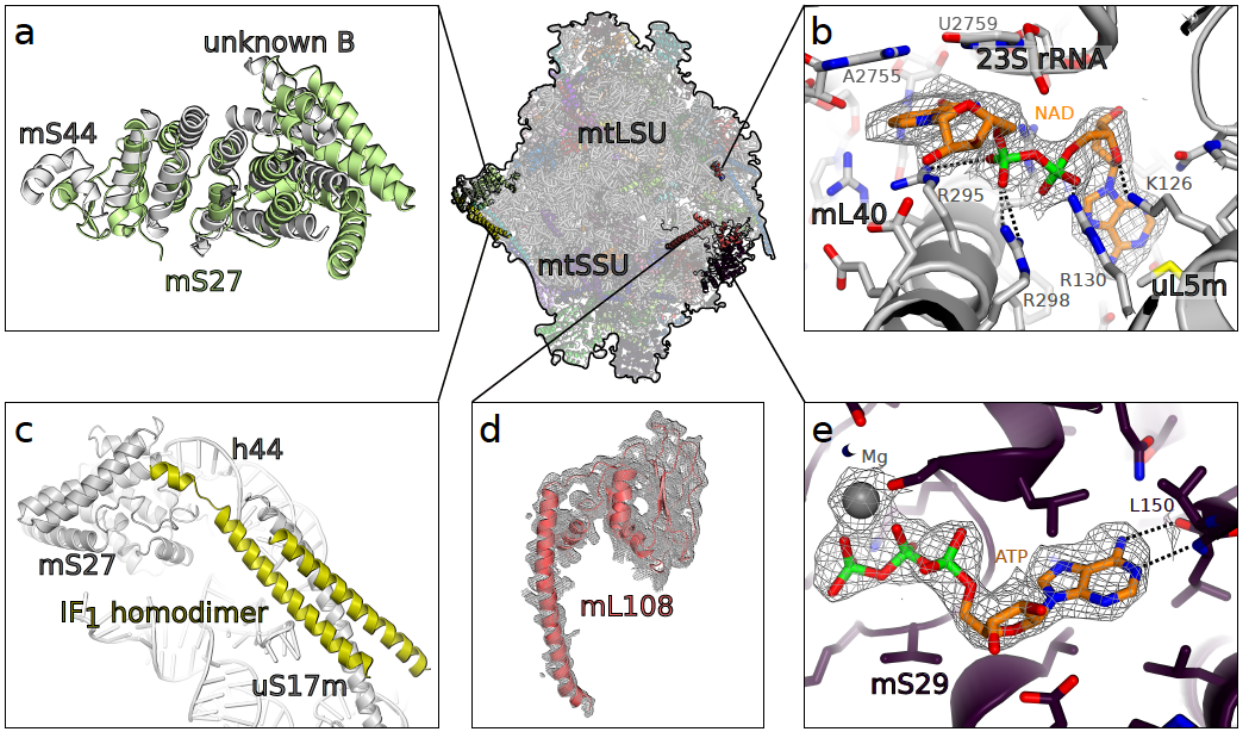

Figure 2: Structural features of the fungal mitoribosome. a, Superposition of the correctly built mS27 the previous model (PDB ID: 5MRC) assigned as mS44 and unknown α-helical protein B. **b,** NAD binding pocket in the CP formed by uL5m, mL40, and H84-ES3. **c,** Newly identified mitoribosomal component IF_1 homodimer bound to h44-ES1 and uS17m extension. **d,** Newly identified mitoribosomal component mL108, located in the L1 stalk, shown with its density. **e,** Nucleotide binding pocket of mS29 bound with chemically favorable ATP shown with its density.

Binding of mRNA to a dedicated protein platform

Focused classifications on the tRNA binding sites yielded structures of three distinct classes with bound tRNA in P/P, P/E, E/E (Fig. 4a). The quality of the density allowed us to generate structural models for the translating mitoribosomal complexes with P/P and P/E tRNAs. The E/E tRNA shows high flexibility especially in the anticodon arm. The presence of tRNAs correlates with additional density lining the mRNA channel path, where 10 nucleotides of mRNA were modeled. The codon-anticodon base pairings are directly observed in the density of both, the P/P and P/E states (Fig. 3). The decoding center is conserved, including the position of the flipped-out bases A1803, A1804, and G756 (A918, A919, and G530 in *E. coli*), and mRNA curves near h28. In addition to the modeled mRNA nucleotides, bulky density above the noise level clearly extends to the channel entry and exit. Therefore, the full mRNA path on the mitoribosome can now be traced from our experimental data (Fig. 3a).

The entry site to the channel is formed by uS3m, uS4m, uS5m, and mS35 (Fig. 3a). Prior the entry, the extensions of uS3m and uS5m are held together at the mtSSU head by mS35 and mS46,

forming a dedicated platform for mRNA loading on to the mitoribosome. This platform narrows the entry site considerably, ensuring that the mRNA entering the channel is in unpaired.

The exit site resides at the 3′ end of the rRNA as in bacteria and is therefore has not been significantly altered. The remodeling reported in *S. cerevisiae* does not occur, and therefore either it represents a dormant state or a species-specific feature. In addition to the conserved proteins, mS23, mS26, and mS37 are added (Fig. 3c). At the inner exit site, the C-terminal extension of uS7m narrows the channel (Fig. 3c). The outer section is split by bS1m, bS18m, and mS23 into two paths, and each could in principle accommodate a single stranded mRNA. However, the density for the 5′ mRNA follows only the path lateral to mS26 that is also surrounded by a positively charged chemical environment (Fig. 3c).

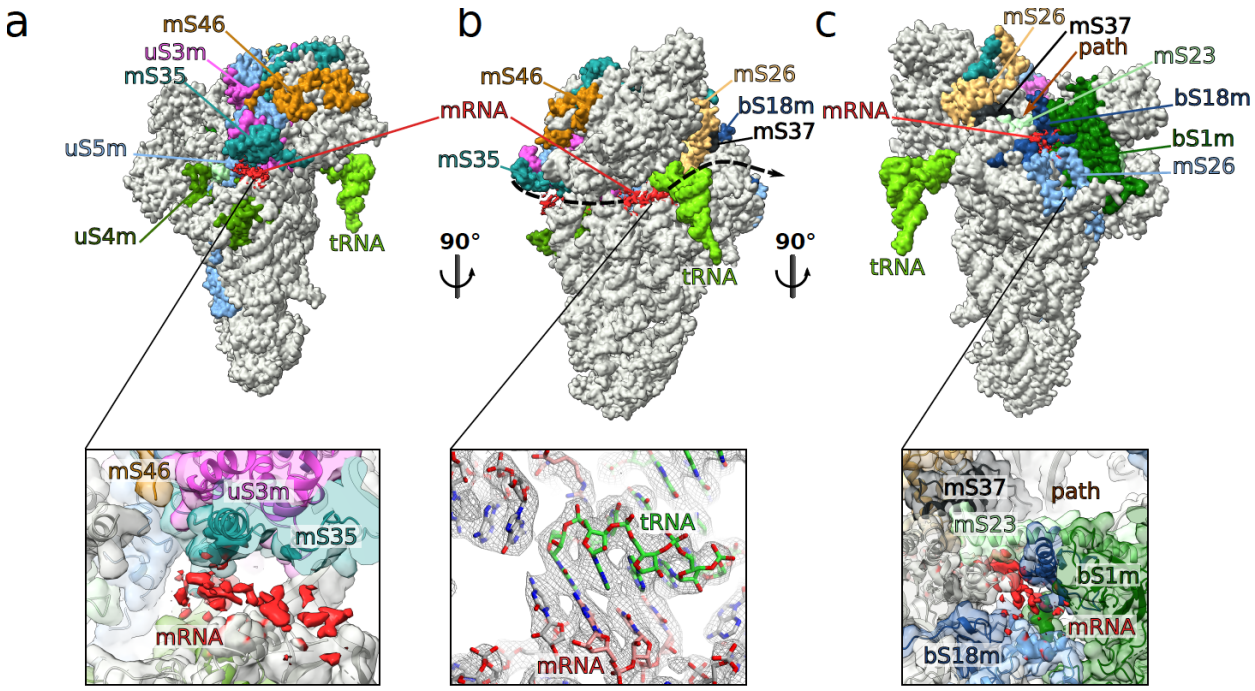

Figure 3: The tRNA states and mRNA path. The mtSSU and tRNA in the P/P state are show as surface model. The density of mRNA path is shown in red color.

Mechanism of tRNA translocation and new protein in L1 stalk

During translation, tRNAs are translocated between the three sites. Upon peptide-bond formation, the ribosomal subunits rotate with respect to each other, and the tRNA moves to the intermediate hybrid state. The structure comparison between the complexes with P/P and P/E tRNAs reveals sequential rearrangements in the network of mitoribosome-tRNA interactions.

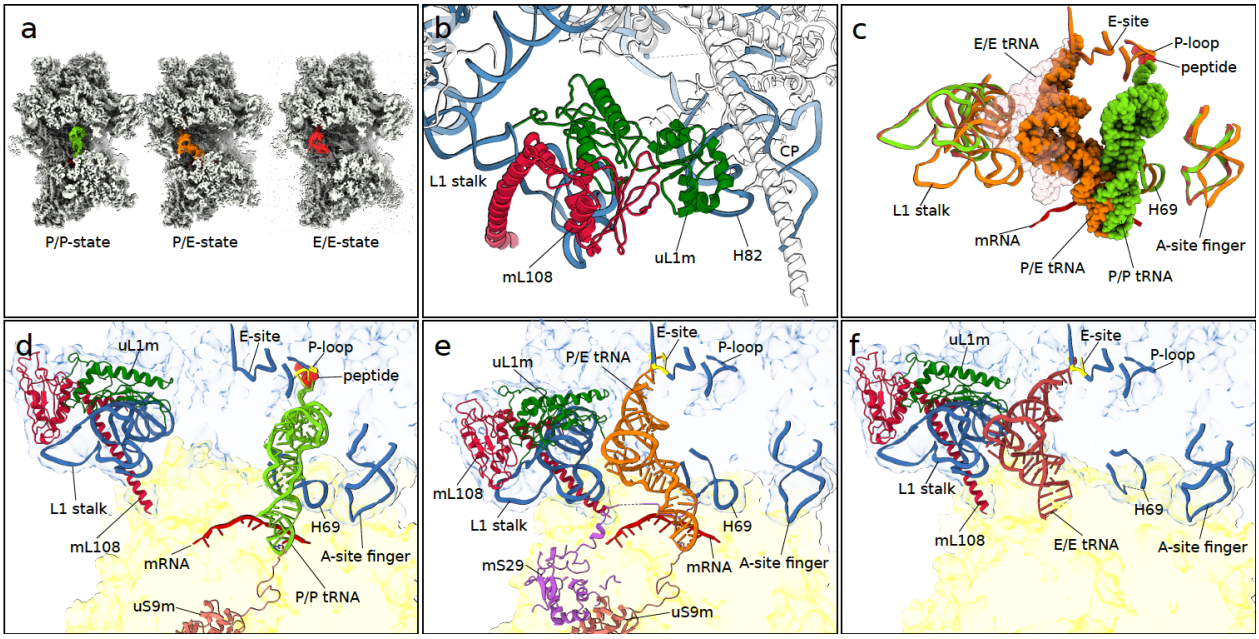

Figure 4: The L1 stalk and translocation of tRNA. a, 3D reconstructions of the three tRNA bound states. **b,** The L1 stalk in the P/E tRNA state with the proteins uL1m and mL108. The insertion domain of uL1m interacts with an expansion of H82 in the CP. **c,** Superposition of the tRNA states showing the movement of tRNAs through the inter-subunit space. P/P, P/E, and E/E states are colored green, orange, and red, respectively. The E/E tRNA is show with transparency for clarity. **d,e,f,** The tRNAs and the L1 stalk in the P/P (D), P/E (E), and E/E (F) states. The N-terminal loop of mS29 interacts only to the P/E tRNA.

In the P/P state the anticodon of the tRNA forms base pairing with the mRNA in the conserved P-site of the mtSSU (Fig. 4d). Further stabilization is provided by the conserved C-terminal Arg15 of uS9m, which forms salt bridges with the backbone phosphates in the anticodon loop of the tRNA. The conserved H69 of mtLSU interacts with the D-arm of the tRNA. The conformation of P/P tRNA is overall similar to bacteria.

The A-site finger, known as a functional attenuator and important for keeping the correct reading frame (Komoda, Sato et al. 2006), takes in a straight conformation forming the inter-subunit bridge B1a. The conserved G2453 and G2454 of the P-loop form base pairs with the CCA terminus of the tRNA and the emerging peptide is bound to the terminal A76, waiting for peptidyl transfer to the next incoming aminoacyl-tRNA at the A-site. Thus, the arrangement of structural elements and tRNA in mitochondria of fungi shows conserved P-site.

After peptide transfer occurred, the ribosomal subunits move relative to each other forming ratcheted conformation coupled with tRNA translocation, which is represented by our P/E hybrid structure. In the ratcheted conformation, the L1 stalk moves to a closed conformation toward the deacylated tRNA in the P/E hybrid state (Fig. 4e). By masked refinement on L1 stalk, we improved the density that allowed building its complete model for the first time in any mitoribosome (Fig. 4b). We identified additional protein component, namely mL108 (Fig. 2d), which is unprecedented occurrence in cytoplasmic counterparts. The protein mL108 interacts

with both the L1-stalk rRNA and the protein uL1m (Fig. 4b). Furthermore, it forms a new inter-subunit bridge with a long C-terminal helix (Fig. 4d-f). The core of the protein shows a thioredoxin-like fold, which belongs to a small folding family including mS25, mL43, and the complex I subunit NDUFA2/B8. These proteins are specific to mitochondria, bearing the possibility of a shared evolutional origin.

The bases A2381 and C2348 of the stalk rRNA stack on the elbow of the P/E tRNA (Fig. 4e). Unlike in bacteria, uL1m does not interact with the P/E tRNA, instead the insertion domain of uL1m changes its conformation to form a mitoribsome specific interaction with H82-ES1 in the CP in the ratcheted state (Fig. 4b). Therefore, the subunit rotation is synchronized with the L1 stalk movement during tRNA translocation. The terminal adenosine of the P/E tRNA inserts between the conserved G2873 and A2874 at the E site (Fig. 4e). The anticodon arm of the tRNA remains located in the P site forming the codon-anticodon base pairing with the mRNA, resulting in distorted conformation, to swing the acceptor arm into the E-site. The disordered N-terminal extension of mS29 gets structured in the ratcheted state and inserts into the groove of the anticodon stem of the P/E tRNA, suggesting mitochondria-specific regulation of the translation mechanism. The long C-terminal helix of mL108 reaches down to the mtSSU, applying additional stabilization of the L1 stalk.

Upon back rotation of the mtSSU into the non-ratcheted E/E state, the L1 stalk moves outwards assisting to pull the P/E tRNA into the E/E state, allowing dissociation into the solvent to complete the translocation cycle (Fig. 4f). The protein uL1m thereby detaches from the CP, releasing the insertion domain of uL1m. The tip of the C-terminal helix of mL108 translates ~20 Å forming a new bridge with mtSSU by slightly changing its curvature. This structural rearrangement during mtSSU rotation suggests for a mitochondria-specific ratchet sensing mechanism that coordinates the movement of the mtSSU rotation via mL108 to the L1 stalk.

Taken together, the data enables to derive a mechanism for the tRNA translocation describing a series of key conformational changes of the mitoribosomes and its ligands. First, the L1 stalk interacts with mtSSU through mL108 thereby sensing the rotation state. This leads to the inward moving of the rRNA part of the L1 stalk to interact with the tRNA. The insertion domain of uL1m stabilizes the conformation through the mitochondria-specific interactions with the CP, and mS29 N-terminal loop becoming ordered and stabilizes the tRNA in the P/E state, which is disrupted in the following E/E state.

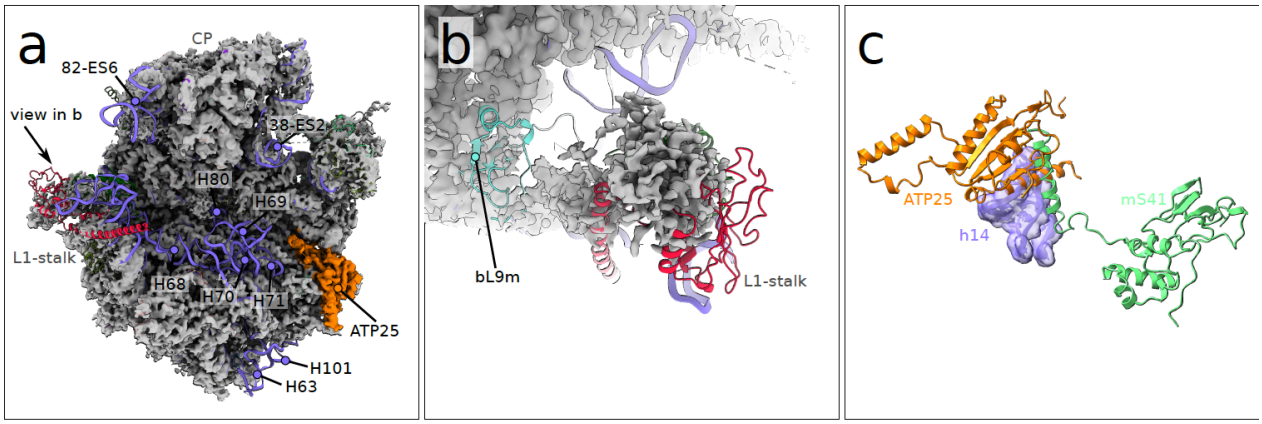

Figure 5: A: mtLSU-Atp25 complex. a, Overall cryo-EM map superposed with the mtLSU model from the intact monosome. Extra density corresponding to Atp25 is colored orange. b, Zoom-in view of the L1 stal. C, Atp25 with h14 and mS41 from the superposed mtSSU are shown to visualize the steric hindrance.

Visualization of mtLSU-Atp25 assembly intermediate

During 3D classification, we recognized a minor population of the particles corresponding to the isolated mtLSU, and subsequent processing resulted in 3.03 Å resolution reconstruction from 24,142 particles. Fitting the mtLSU model revealed extra density that appears as a protein element forming heterodimer with uL14m. In addition, rRNA at the interface (38-ES2, H63, H67-71, H80, 82-ES6, H101, PTC) appeared as unfolded (Fig. 5a). Further, the L1 stalk changes to conformation that is more flexible and the density for bL9m next to L1 stalk is absent (Fig. 5b), whereas all the other mtLSU proteins are present.

We identified the extra density as Atp25, an ortholog of the bacterial ribosome silencing factor (Rsf), for which there is no high-resolution structural information in complex with ribosome (Häuser, R. et al. PLoS Genet. 8, e1002815 (2012); Li, X. et al. Structure 23, 1858–1865 (2015). Its human mitochondrial counterpart MALSU1 has been shown to involve late assembly stages Rorbach, et al Nucleic Acids Res. 40, 4097–4109 (2012); Brown et al. 2017 NSMB). The *Atp25* sequence codes for 699 amino acids, including the targeting sequence, N-terminal part related to Rsf/MALSU1, and C-terminal part called the M-domain. In *S. cerevisiae*, the M-domain is cleaved during mitochondrial import (Woellhaf, Sommer et al. 2016), to form a separate functional protein that stabilizes the mRNA of the ATP synthase subunit Atp9p (Zeng, Barros et al. 2008). The gene fusion is suggested to have evolved in order to prevent off target effects of Atp25 on the cytosolic ribosomes prior entry to mitochondria (Woellhaf, Sommer et al. 2016). We modeled 186 residues Atp25 on the mitoribosome, confirming the function in the assembly of the mtLSU.

Visualization of the mtLSU-Atp25 complex provides the structural basis for the assembly pathway and insight into possible regulation of translation in mitochondria. Atp25 presents only in the class with the missing bL9m and unfolded interfacial rRNA that affects the L1 stalk. In the mature mitoribosome, bL9m is anchored at the base of the L1 stalk near the E-site, which is stabilized through tertiary interactions with the rRNA. Therefore, the recruitment of bL9m requires specific L1 stalk conformation that is interdependent with rRNA folding, including the PTC. Indeed, ribosomes purified from bL9-deficient strain of *Escherichia coli* show increased susceptibility to aminoglycosides (Naganathan, M. P. Wood, S. D. Moore, (**30**), and the folding of the PTC is among the last maturation events (Li, N. et al. Nucleic Acids Res. 41, 7073–7083 (2013);. Jomaa, A. et al. Nucleic Acids Res. 42, 3419–3435 (2014). Furthermore, bacterial ribosomes lacking bL9 exhibit increased frameshifting (**1**, **28**, **29**), for which the molecular mechanism has been proposed recently through transiently stalled compacted ribosomes (Smith et al 2019 https://doi.org/10.1073/pnas.1910613116). Atp25 bound to uL14m sterically obstruct the binding of the mtSSU by preventing the formation of bridge B8 with its globular domain (Fig. 5c). The steric block spans ~25 Å, would clash with h14 of rRNA and the N terminus of mS26 of the mtSSU. Therefore, the eviction of Atp25 must take place during the final stages of maturation to alleviate the steric hindrance on subunit joining. A similar mechanism was proposed for eIF6 in the cytoplasmic translation apparatus, where protein factor SBDS senses the structural integrity of the functional sites before the displacement (Weis, F. et al. Mechanism of eIF6 release from the nascent 60S ribosomal subunit. Nat. Struct. Mol. Biol. 22, 914–919 (2015). Our data imply that since this is a prerequisite step for the folding of interfacial mt-rRNA into a native-like conformation, it is also a requirement for the binding of bL9m. This shows that bL9m assembly is mechanistically regulated during the assembly of the mitoribosome. Since bL9 suppresses frameshifting in bacteria, the structure of the mtLSU-Atp25 lacking bL9m suggests regulation of frameshifting in mitochondrial translation, which might be important for fidelity and reflects the adaptation to the mitochondrial mRNAs.

References

Methods

Isolation of mitochondria

Mitochondria were isolated from *Neurospora crassa* strain K5-15-23-1 (Funes, Nargang et al. 2004) which contains a His-tagged version of Oxa1. The *N. crassa* mycelia were grown in aerobic conditions using 10 L of the Vogel's growth medium (Vogel 1956), supplemented with L-lysine and L-leucine at 25°C for 16 h. Each growth flask was supplemented with chloramphenicol (1:1000) 1 h prior to harvesting. To separate the moisture from the mycelia, the culture was filtered through muslin. The dry mycelia were transferred to a pre-cooled mortar and pestle to lyse the cells. All further operations were performed at 4°C. The cells were lysed using sea-sand (silicon dioxide) and SEMP buffer (250 mM sucrose, 1 mM ethylenediaminetetraacetic acid (EDTA), 10 mM MOPS-KOH pH 7.2, 2 mM phenylmethanesulfonyl fluoride (PMSF), and 1:500

329 chloramphenicol), by applying a 20 min grinding course. Sand and cell debris were removed us-
330 ing differential centrifugation at low-speed (2000 x g). A subsequent high-speed centrifugation
331 step (17,500 x g) was carried out to sediment crude mitochondria. The mitochondrial pellet was
332 then resuspended in SEM buffer (250 mM sucrose, 1 mM EDTA, and 10 mM MOPS-KOH pH
333 7.2). To further purify, the crude mitochondria were undergone a sucrose gradient in SEM buffer
334 for 1h at 28,000 rpm with an SW40 Ti rotor (Beckman Coulter). Mitochondrial band was pooled
335 and stored at -80 °C.

336

337 **Purification of mitoribosomes**

338 Mitochondria were lysed in 4 volumes of lysis buffer (25 mM Hepes-KOH pH 7.5, 20 mM KCl,
339 15 mM $Mg(OAc)_2$, 2% *n*-dodecyl-β-D-maltoside (DDM), 0.0075 % cardiolipin, 2 mM dithio-
340 threitol (DTT), 1 tablet of protease inhibitor (cOmplete^{TM}, Roche), and RNase inhibitor
341 (RNaseOUT, Invitrogen)) and incubated for 5 min at 4°C. The membrane was separated by cen-
342 trifugation of the mitochondrial lysate at 30,000 x g for 20 min followed by a second centrifuga-
343 tion step with the same settings. The supernatant was loaded onto a 1.0 M sucrose cushion in the
344 resuspension buffer (20 mM Hepes-KOH pH 7.5, 15 mM KCL, 15 mM $Mg(OAc)_2$, 0.05% DDM,
345 0.0075% cardiolipin, and 2 mM DTT) with RNase inhibitor and centrifuged at 48,000 rpm with a
346 70 Ti rotor for 4 h. The pellet was then resuspended in the resuspension buffer, loaded on a 15-
347 30% sucrose gradient in the resuspension buffer, and centrifuged at 23,000 rpm with an SW40 Ti
348 for 16 h at 4°C. Fractions containing mitoribosomes were collected and the mitorobosomes were
349 pelleted by centrifugation at 100,000 rpm with a TLA120.2 rotor (Beckman Coulter) for 45 min
350 at 4°C and resuspended in the resuspension buffer.

351

352 **Cryo-EM and image processing**

353 Freshly purified sample was used for grid preparation. 3 µl aliquots of purified mitoribsomes was
354 incubated for 30 s on glow-discharged holey carbon grids (Quantifoil R2/2, 300 mesh, copper)
355 pre-coated with a home-made continuous carbon film with thickness of ~ 27 Å. The grids were
356 thereafter vitrified in a liquid ethane with a Vitrobot MKIV (FEI/Thermo Fisher) using a blotting
357 time of 3 s at 4°C and 100% humidity. Micrographs were collected with a 300 kV Titan Krios
358 (FEI/Thermo Fisher) transmission electron microscope, 70 µm C2 aperture, using a slit width of
359 20 eV on a GIF-Quantum energy filter (Gatan). A K2 summit detector (GATAN) was used in the
360 counting mode at the calibrated magnification of 130,000 (yielding a pixel size of 1.06 Å). An
361 exposure time of 9 s yielding a total of 35 e/Å^2 was dose fractionated into 20 frames. In total
362 3,172 movies were collected automatically during two consecutive days using EPU (FEI/Thermo
363 Fisher) data collection software. Defocus values ranged between 0.8 and 3.0 µm.

364 Collected movie frames were aligned and corrected for both global and non-uniform local beam-
365 induced movements using MotionCor (Li, Mooney et al. 2013) and the contrast transfer function
366 (CTF) parameters were estimated using Gctf (Zhang 2016), inside the SCIPION program (de la
367 Rosa-Trevín, Quintana et al. 2016). Subsequent data processing steps were performed using

368 RELION-2.1 and 3.0 (Kimanius, Forsberg et al. 2016). First, 647 particles were manually picked,
369 followed by two-dimensional (2D) classification. Four good 2D class averages were used for ref-
370 erence-based picking for the second round. 265,710 picked particles were subjected to 2D classi-
371 fication and 50 good 2D classes were selected (Figure S1A). Retained 223,605 particles were
372 classified into six classes by three-dimensional (3D) classification, resulted in four good mito-
373 monosome classes (131,806 particles), one class with weak mtSSU density (36,053 particles),
374 and one low quality class containing junks. From the class with weak mtSSU density, isolated
375 mtLSU particles (24,142 particles) are classified out by further 3D classification.

376 Pooled good particles were subjected to 3D auto-refinement. Per particle CTF refinement
377 (Zivanov, Nakane et al. 2018), followed by Bayesian polishing (Zivanov, Nakane et al. 2019)
378 and the second round of per particle CTF refinement to improve resolution, resulted in recon-
379 structions of mito-monosome and the isolated mtLSU with 2.83 and 3.03 Å resolution, respec-
380 tively (Figure S1A). Resolution is estimated based on the gold standard criterion of Fourier shell
381 correlation (FSC) = 0.143 between the reconstructed two half maps.

382 Due to the relative movement between the mtSSU and mtLSU in monosome, we suffered from
383 low resolution in the mtSSU. We therefore decided to improve the quality of the maps by focused
384 masked refinement for the mtSSU and mtLSU separately. We obtained the masked maps of
385 mtLSU and mtSSU with 2.74 and 2.85 Å resolution, respectively (Figure S1A). Further, im-
386 provement of local resolutions was achieved by focused refinement using the local masks shown
387 in Fig.S1B.

388 All the density maps were locally resolution filtered by applying a negative B-factor estimated
389 automatically by RELION-3.0.

390

391 **Classification of the tRNA states**

392 The observed motion between mtLSU and mtSSU prompted us to separate possible sub-states of
393 the monosome. Firstly, we classified the particles in two major classes (ratcheted and non-
394 ratcheted states) by overall 3D classification (Fig.S1A). To facilitate classifying tRNA states,
395 signal subtraction of ribosome was performed using a cylindrical mask covering the A-, P-, and
396 E-sites for the ratcheted and non-ratcheted states separately by RELION 3.0, following by
397 focused 3D classification without alignment. For the ratcheted state, the same cylindrical mask
398 was applied for the classification, which separated the P/E hybrid tRNA bound mitoribosomes
399 (37,908 particles). For non-ratcheted state, smaller masks were needed to classify tRNAs. The
400 P/P tRNA bound mitoribosomes were separated applying a mask covering only the P-site, while
401 E/E tRNA bound ones were separated by a mask covering only the E-site (Fig.S1A). The P/P
402 tRNA and E/E tRNA bound mitoribosomes were 24,611 and 23,802 particles, respectively.
403 Among them, only 4,136 particles are overlapping and have both P/P and E/E tRNAs, which are
404 too few for high-resolution reconstruction.
405 Local resolution of the tRNA bound mitoribosomes were also improved by using local masked
406 refinement as shown in the scheme depicted in Fig.S1C.
407

408 **Model building, refinement, and deposition**

409 Model building was carried out in Coot (Emsley and Cowtan 2004). Rigid body docking was car-
410 ried out in UCSF Chimera (Pettersen, Goddard et al. 2004). The model of the *S. cerevisiae* mi-
411 toribosome (PDB ID: 5MRC) was used as a reference. For proteins whose orthologs existed in *S.*
412 *cerevisiae* structure, except for mS44, the homology models of *N. crassa* were generated by
413 SWISS Model (Waterhouse, Bertoni et al. 2018), placed into the density, manually revised and
414 built unmodeled and unique regions, and real space fit in Coot. Previously unknown or unmod-
415 eled proteins and mS44 were modeled *de novo* in Coot. mS44 could not be identified from any *N.*
416 *crassa* database due to the low sequence similarity. For the correct assignment of the proteins,
417 sequence stretches of reasonable quality were directly identified from the map and then applied to
418 BLAST (Altschul, Gish et al. 1990) and/or compared to the protein sequences gained from mass
419 spectrometry. The ribosomal protein mL108 was named according to the standard nomenclature
420 widely accepted in the ribosome community (Ban, Beckmann et al. 2014). The number was cho-
421 sen in a chronological order of discover also considering unpublished data. The entire rRNAs,
422 tRNAs, and mRNAs were modeled *de novo* in Coot. Since bound tRNAs and mRNAs are mix-
423 ture of any mitochondrial ones, each residue was assigned as either A, U, G, or C, based on the
424 density and conservation. Ligands and metal ions were placed into the density.

425 For model refinement of the consensus mtLSU and mtSSU and the monosomes in the three tRNA
426 states, the local masked refined maps with B-factor sharpening and local-resolution filtering were
427 merged using the program phenix_combine_focused_maps in the Phenix software suite
428 (Liebschner, Afonine et al. 2019), thereby generating a map for model refinement. For the isolat-
429 ed mtLSU, the overall refined map with B-factor sharpening and local-resolution filtering was
430 used for model refinement. Refinement of all models was performed using Phe-
431 nix.rel_space_refine (Afonine, Poon et al. 2018). The final structure was validated using the
432 MolProbity (Williams, Headd et al. 2018) implementation of the Phenix suite.

433

434 **Figure preparation**

435 All structural figures were generated with PyMOL (DeLano 2002), UCSF Chimera (Pettersen,
436 Goddard et al. 2004), and ChimeraX (Goddard, Huang et al. 2018). The secondary structure dia-
437 grams of the 16S and 23S rRNA were generated using XRNA
438 (http://rna.ucsc.edu/rnacenter/xrna/xrna.html). The peptide and mRNA tunnel was predicted us-
439 ing the software Mole (Sehnal, Svobodova Varekova et al. 2013).

440

441

442

443 **Acknowledgements** We thank Frank Nargang for providing the *N. crassa* strain, and Marta
444 Carroni and Julian Conrad for supporting cryo-EM data collection. This work was supported by
445 the Swedish Foundation for Strategic Research (FFL15:0325), Ragnar Söderberg Foundation
446 (M44/16), Swedish Research Council (NT_2015-04107), Cancerfonden (2017/1041), European

Research Council (ERC-2018-StG-805230), Knut and Alice Wallenberg Foundation (2018.0080), EMBO Young Investigator Program. Y.I. is supported by H2020-MSCA-IF-2017 (799399-Itohribo). The data was collected at the SciLifeLab cryo-EM facility funded by the Knut and Alice Wallenberg, Family Erling Persson, and Kempe foundations.

Author contributions A.A. designed the project. N.M prepared the sample and collected cryo-EM data. Y.I., A.N. and N.M. processed the data and built the model. A.N. and A.A. wrote the manuscript with help from Y.I., N.M. and J.H.

Competing interests The authors declare no competing interests.

458 **Supplementary Tables S1-S2**

459 **Table S1. List of RNA and proteins from mt-LSU.**

Name	Gene	Uniprot ID	Chain ID	Modeled	Size	Notes
23S rRNA	–	–	A		3464	Spermine bound next to A1271.
uL1m	MRPL1	Q1K699	e	59–300	303	Conserved in *S. cerevisiae* and human but disordered in their structures.
uL2m	RML2	Q7SCX7	B	54–379	383	Likewise its *S. cerevisiae* counterpart, NT extension locates at the subunits interface.
uL3m	MRPL9	Q1K8T6	C	63–369	384	A helix at CT extension is similar to the human uL3m. This extension does not exist in the *S. cerevisiae* counterpart.
uL4m	YML6	V5IMN1	D	62–302, 312–324	325	
uL5m	MRPL7	Q1K6P0	E	44–352	352	
uL6m	MRPL6	Q7RZF0	F	52–252	255	
bL9m	MRPL50	Q7S054	G	52–125	300	
uL10m	MRPL11	Q7RZ62	f	54–298	347	Conserved in *S. cerevisiae* and human. It is not modeled in the *S. cerevisiae* structures.
uL11m	MRPL19	Q7RX40	g	12–158	158	Conserved in *S. cerevisiae* and human. It is not modeled in the *S. cerevisiae* structures.
uL13m	MRPL23	Q7SBV6	H	1–183	183	
uL14m	MRPL38	Q7SBJ8	I	1–46, 59–130	131	
uL15m	MRPL10	Q7SB98	J	47–289	312	
uL16m	MRPL16	F5HIJ5	K	61–228	249	
uL17m	MRPL8	Q1K8C8	L	2–193	193	CT extension unlike its *S. cerevisiae* counterpart lacking a helix.
bL19m	IMG1	Q7RYW8	M	41–234	258	
bL21m	MRPL49	Q7SGE5	N	85–217	217	
uL22m	MRPL22	Q7S5N0	O	43–71, 122–364	364	NT extension extensively remodeled with respect to its *S. cerevisiae* counterpart, whereas CT extension is quite similar. NT partially occupies the position of the absent bacterial rRNA helix 24.
uL23m	MRP20	Q7SA60	P	13–192	228	CT extension remodeled respective to its *S. cerevisiae* counterpart. Most likely it does not block the bacterial exit tunnel likewise CT extension in *S. cerevisiae* uL23m.
uL24m	MRPL40	Q7RXU7	Q	1–353	396	NT extension is a long helix that is not like its bacterial, *S. cerevisiae*, and human counterparts. CT extension is similar to that of the *S. cerevisiae*; it covers a long distance through the surface thereby connecting different parts of the large subunit. The CT extension compensates the absence of bacterial helices 15 and 16.
bL27m	MRP7	Q1K730	R	75–196, 248–383	447	NT extension is similar to bacterial, *S. cerevisiae* and human counterparts. CT extension extensively remodeled respective to *S. cerevisiae* bL27, and partially interacts with rRNA helix 82.
bL28m	MRPL24	Q7SC44	S	42–203, 209–225	274	CT extension remodeled extensively respective to *S. cerevisiae* counterpart.
uL29m	MRPL4	Q7S910	T	44–223	263	
uL30m	MRPL33	Q1K8Y7	U	2–102, 125–161	161	
bL31m	MRPL36	Q1K7L7	V	48–128, 189–207	219	Bridging the LSU CP and the SSU head.
bL32m	MRPL32	Q1K4P1	W	64–122	129	Zn binding

bL33m	MRPL39	V5IM60	X	7–54	59	
bL34m	MRPL34	Q96U95	Y	95–140	140	
bL36m	RTC6	Q7S4E7	0	79–124	124	Zn binding
mL38	MRPL35	Q7RXV8	1	83–449	449	CT extension partially compensates the absence of bL35. Stabilizes helices 84-ES and 82-ES.
mL40	MRPL28	V5IQE0	2	251–370	370	Stabilize helices 82-ES, 84-ES, 38-ES1. NAD is binding and interacting with mL40
mL41	MRPL27	Q7S5W0	3	9–103	103	
mL43	MRPL51	Q7S300	4	2–138	138	
mL44	MRPL3	Q7SA88	5	55–235 273-439	439	NT extension slightly remodeled respective to *S. cerevisiae* mL44. CT extension interacts with helix 0-ES1. It forms heterodimer with mL57.
mL46	MRPL17	Q7S1Z3	6	81–245 253-303 311-368	368	Interacts with helices 38-ES1 and 82-ES.
mL49	IMG2	Q7S518	7	82–165	165	Most likely interacts with helix 28.
mL50	MRPL13	Q7S711	8	273–296, 303–442	443	Extensively remodeled. A 31 amino-acid long helix at the solvent-exposed surface of the protein. Interacting with helices 45 and 46.
mL53	MRPL44	Q7SGH0	h	1–98	98	Conserved in *S. cerevisiae* and human. It is not modeled in the *S. cerevisiae* structures.
mL54	MRPL37	Q7SCZ3	i	77–118, 138–218	218	Bridges L10/L11 area to CP. Conserved in *S. cerevisiae* and human. It is not modeled in the *S. cerevisiae* structures and only one helix is modeled in the human structures.
mL57	MRPL15	Q7S1R6	9	61–265	267	Forms a heterodimer with mL44. Stabilizes helix 0-ES1.
mL58	MRPL20	Q1K6U7	a	41–103, 129–225	225	Interacts with helix 0.
mL59	MRPL25	Q7SEK9	b	2–162	162	
mL60	MRPL31	U9W8F2	c	13–110	110	
mL67	MHR1	Q7RYM5	d	33–218 243-291	292	Similar to its *S. cerevisiae* counterpart with slight remodeling at NT and CT extensions.
mL108		Q7RWZ7	j		201	Conserved but not modeled in *S. cerevisiae*
Nascent polypeptide	-	-	XX			

461

462 **Table S2. List of RNA and proteins from mt-SSU.**

MRP	Gene	Uniprot ID	Chain ID	Modeled	Size	Notes
16S rRNA	–	–	a		1864	
bS1m	MRP51	A7UWX2	A		470	
uS2m	MRP4	V5ILE0	B		428	
uS3m	VAR1	P23351	C		508	
uS4m	NAM9	Q7SA90	D		453	
uS5m	MRPS5	Q1K548	E		477	Has a unique insertion to form a unique second beak.
bS6m	MRP17	Q7SB95	F	2–117	117	
uS7m	RSM7	Q7S6M9	G		309	
uS8m	MRPS8	Q7SHF3	H	2–161	161	
uS9m	MRPS9	Q7S7R6	I		315	
uS10m	RSM10	Q7RYL4	J		268	
uS11m	MRPS18	Q7SGU0	K		376	
uS12m	MRPS12	Q7S9I4	L		174	
uS13m	SWS2	Q7S2C2	M	2–119	119	
uS14m	MRP2	Q7SF85	N	2–113	113	
uS15m	MRPS28	Q1K5G1	O		320	
bS16m	MRPS16	P08580	P		107	
uS17m	MRPS17	Q7S4E0	Q		165	A unique C-terminal helix, which binds the ATP IF_1 dimer.
bS18m	RSM18	Q1K8E0	R		256	
uS19m	RSM19	Q1K8V2	S		91	
bS21m	MRP21	Q7SAJ1	T		236	
mS23	RSM25	F8MRK5	U		240	
mS26	PET123	Q7SHR9	V		316	
mS27	MRP13	Q7RYW7	W		396	Corresponds to mS27 in human. In *S. cerevisiae*, mS44 and the unknown B are one connected protein, which corresponds to human and *N. crassa* mS27.
mS29	RSM23 /DAP3	Q7SD06	X		469	DAP3 death associated protein 3. ATP and Mg ion are bound.
mS33	RSM27	Q1K5R0	Y		108	
mS35	RSM24	Q1K5Z0	Z		382	Has a unique N-terminal domain to form a unique beak.

mS37	MRP10	Q7S4Y4	1	2–89	90	
mS38	COX24	Q7SHR6	2	312–344	344	
mS41	FYV4	Q1K6Q3	3		236	
mS42	RSM27 /MRP1	Q7S2H6	4, 5		310	Homolog of Fe superoxide dismutase. Lost the catalytic Fe ion binding side. Two chains form a homodimer, in contrast to the mS42-mS43 heterodimer in *S. cerevisiae*.
mS45	MRPS35	Q7SHB2	6		348	
mS46	RSM28	Q7SG49	7		414	
mS47	MRP5 /EHD3	Q1K7A4	8		508	3-hydroxyisobutyryl-CoA hydrolase. Probably an active enzyme because its active site is conserved.
ATPIF1	INH1	V5IRA3	0, 9		95	ATP synthase inhibitor 1. Forms a homodimer located in the SSU tail region.
tRNA	–	–	b		76	P, E or P/E tRNA state. The density is mixture of tRNA species.
mRNA	–	–	e		–	

463

464

465 **Supplementary Figures**

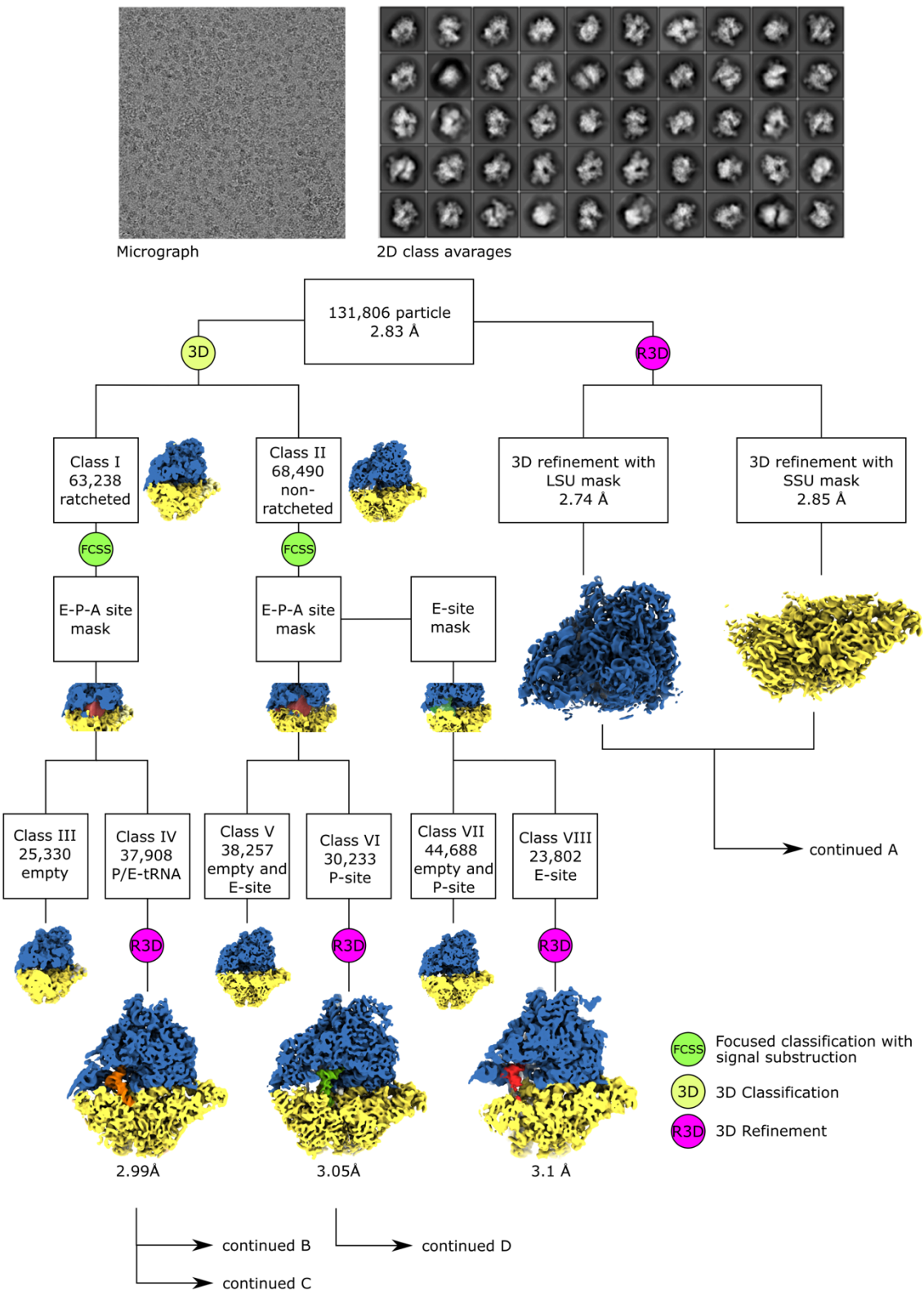

Figure S1A: Top: Representative micrograph and a gallery of the 2D class averages. **Bottom:** Data Refinement protocol and classification scheme for mtLSU, mtSSU and monosomes.

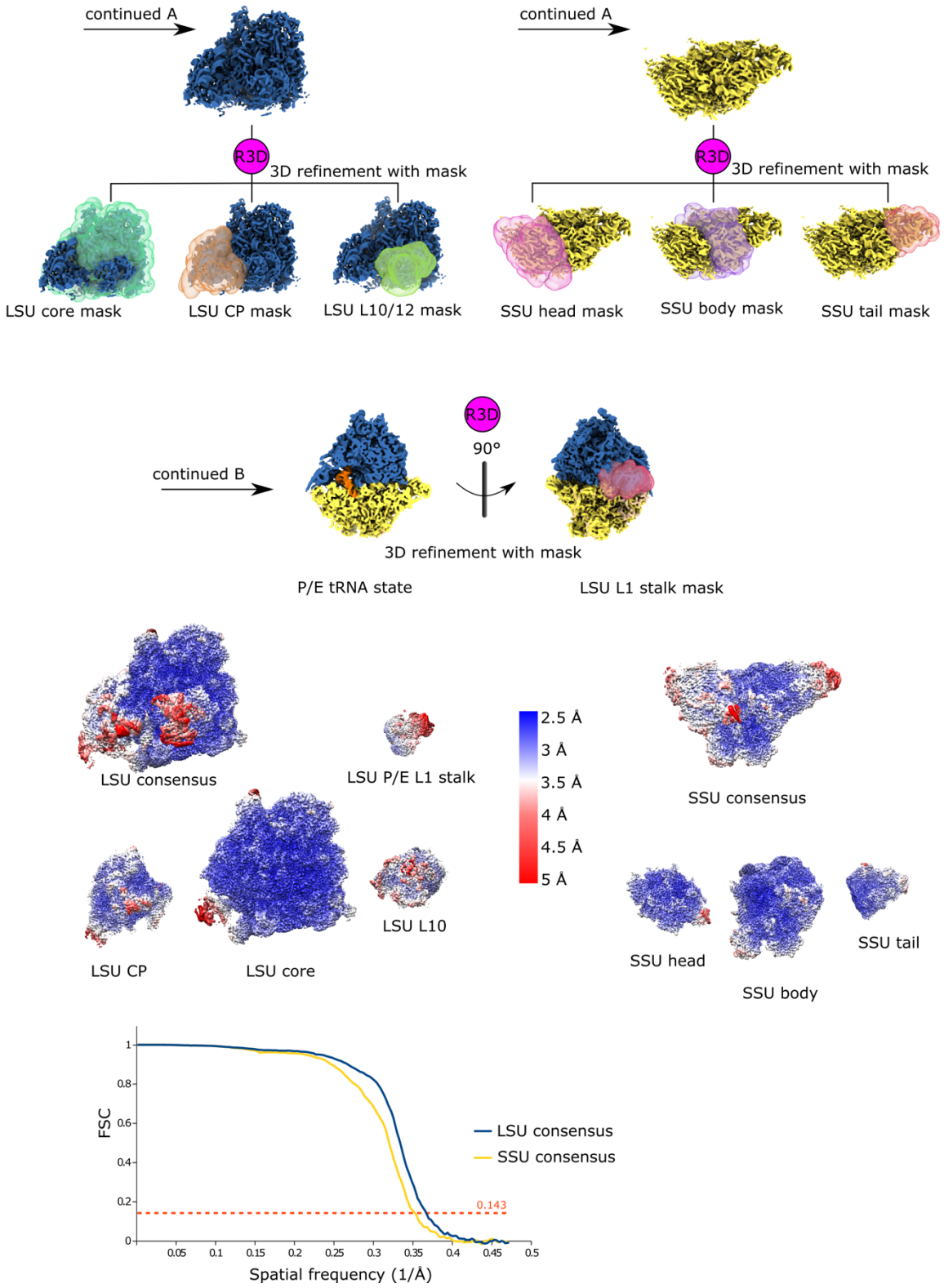

Figure S1B: Top: Continued scheme of Figure S1A showing masked refinement protocol of mtLSU, mtSSU and L1 stalk of P/E tRNA bound state. **Bottom:** Local resolution shown for the consensus maps as well for the masked maps from local regions as indicated. Fourier-shell-correlation (FSC) curves for the consensus maps are shown.

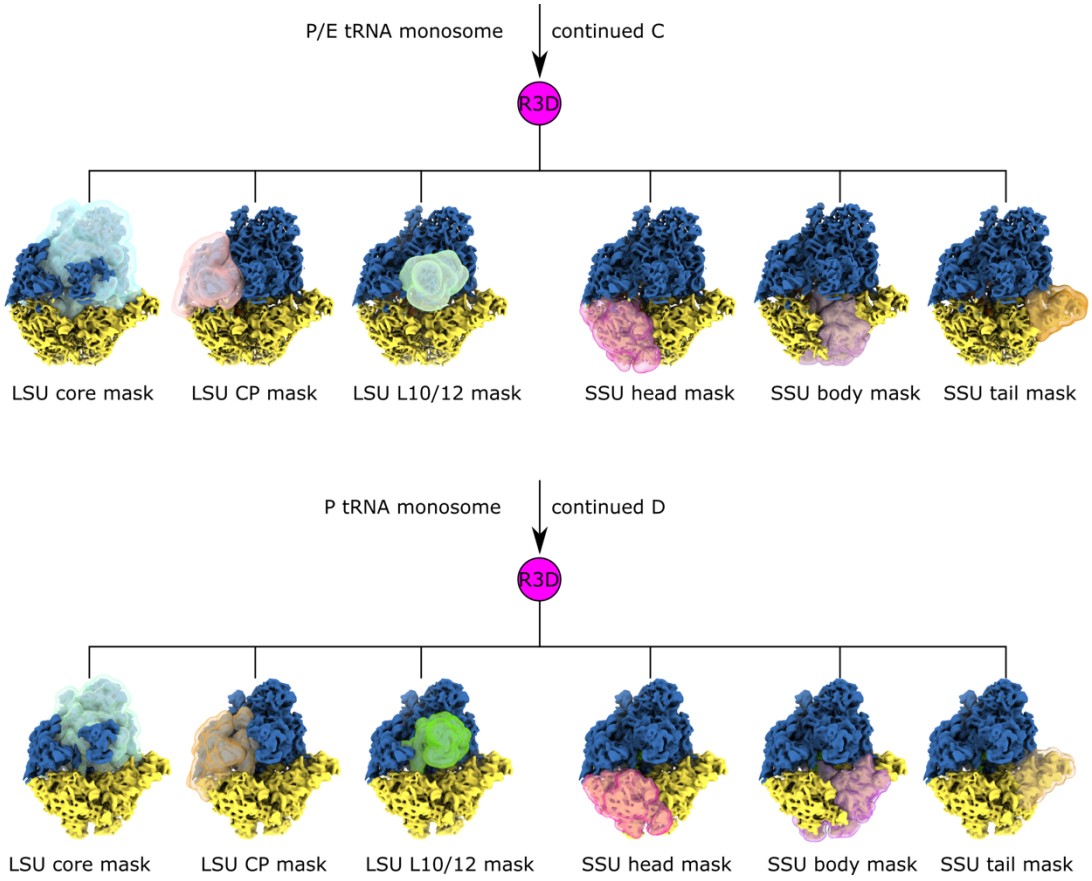

Figure S1C: Continued scheme of Figure S1A showing masked refinement protocol of the P/E tRNA and P tRNA bound states.

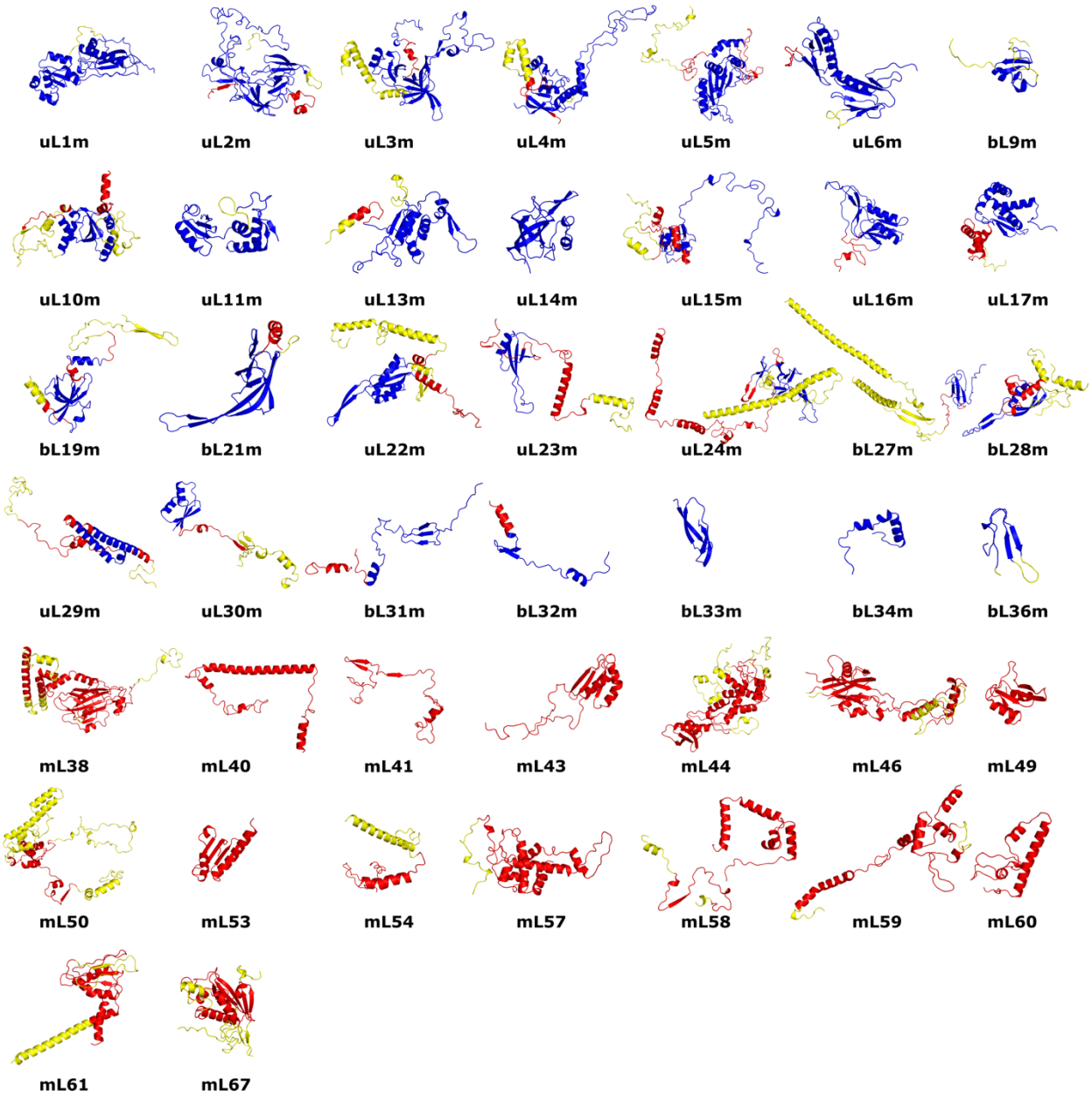

Figure S2A: Expansion elements of mitoribosomal proteins of mt-LSU of *N. crassa*. Tertiary folds of all proteins of the *N. crassa* of the mt-LSU colored by conservation. Elements that are conserved in bacteria are colored in blue. Elements that are shared between *N. crassa* and *S. cerevisiae* are colored in red. Expansions that are unique to *N. crassa* are colored in yellow.

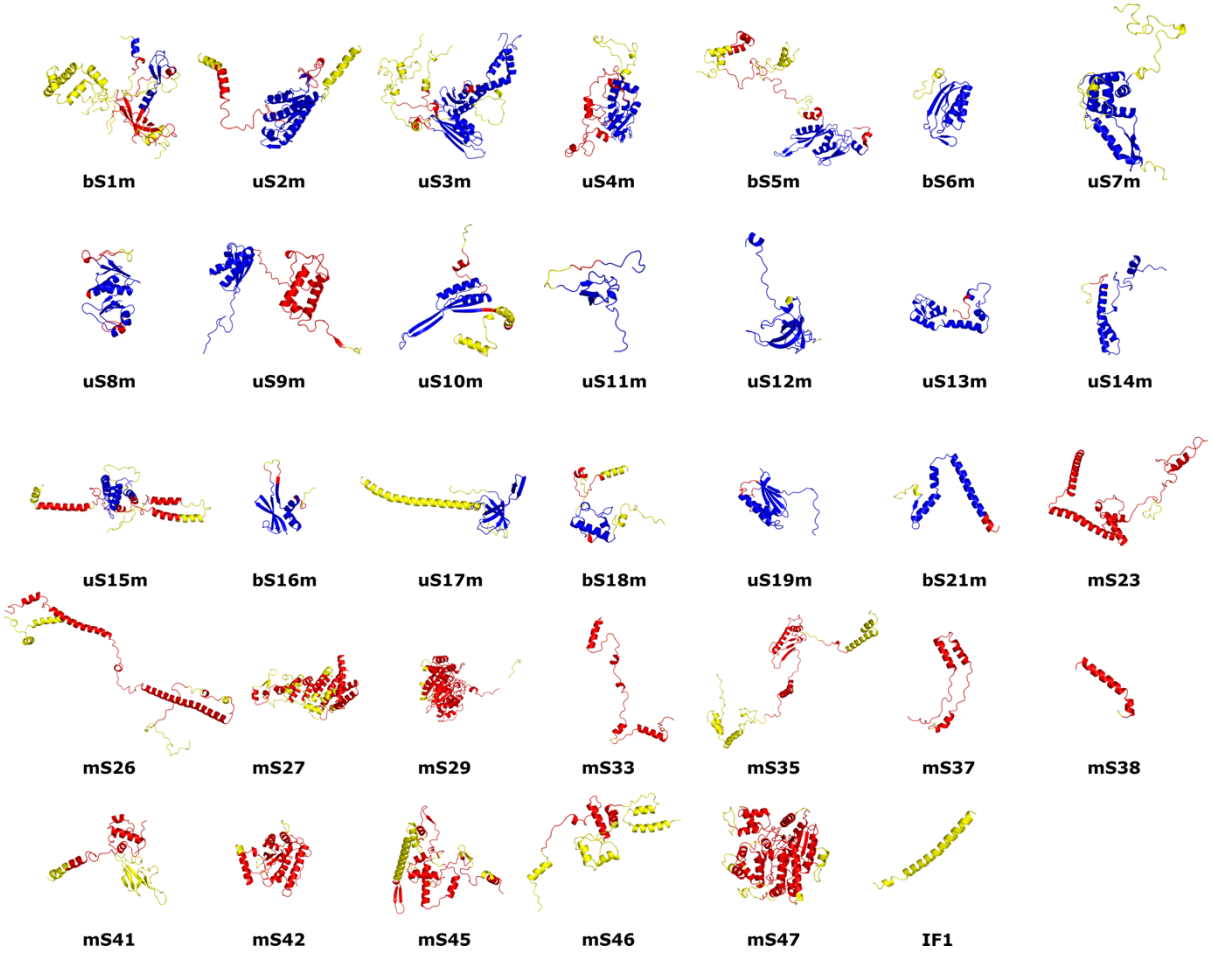

Figure S2B: Expansion elements of mitoribosomal proteins of mt-SSU of *N. crassa*. Tertiary folds of all proteins of the *N. crassa* of the mt-SSU colored by conservation. The same coloring scheme is used as in Figure S3A.

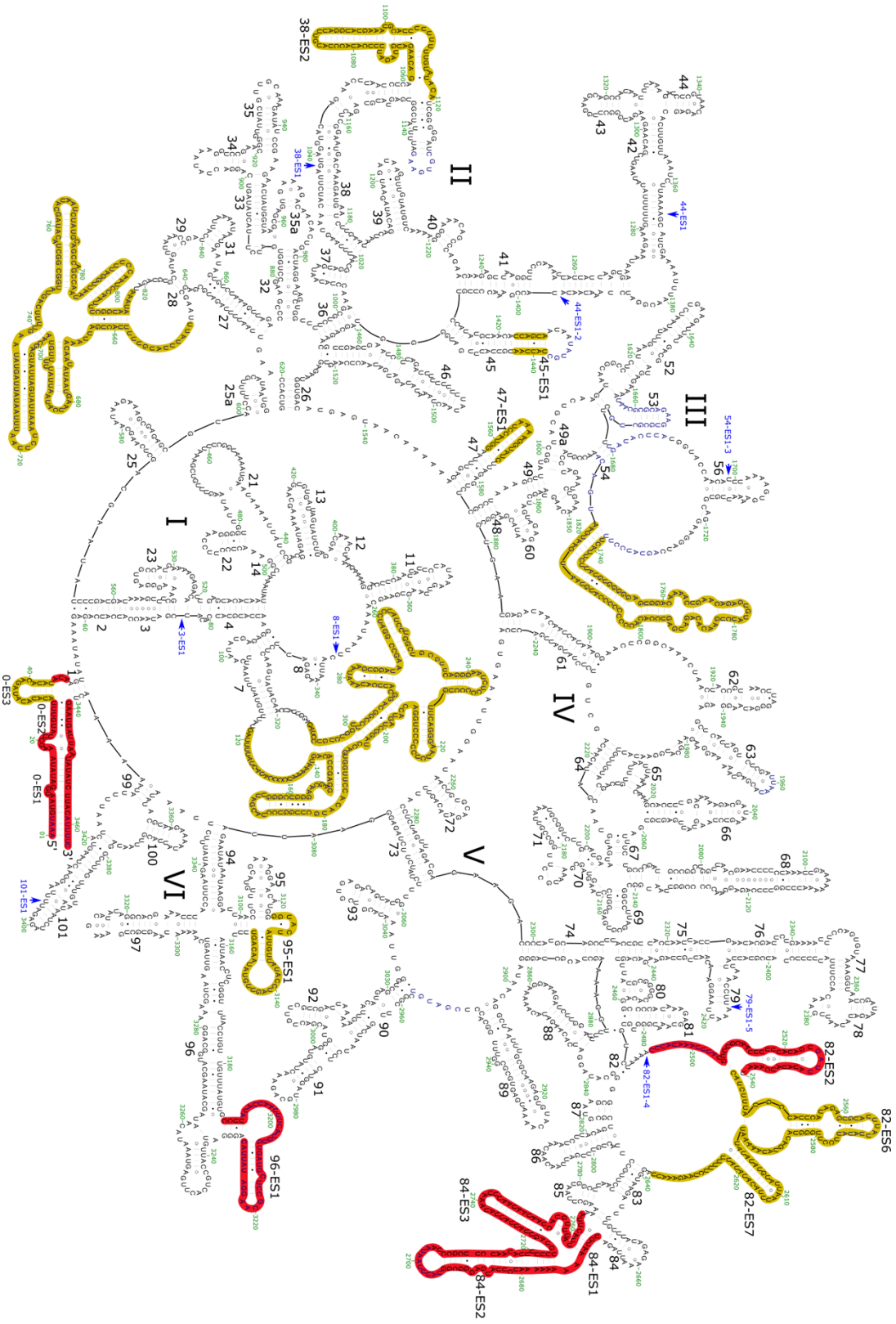

Figure S3A: Secondary structure diagram of the 23S rRNA of the mt-LSU as estimated from the structure. ES unique to *Neurospora* are shown in yellow and ES shared with *S. cerevisiae* shown in red. Regions absent in the structure were predicted

492 and indicated by blue colored bases. Nucleotides are labeled in green and helices are numbered in black. ES absent in *N. crassa*
493 but present in *S. cerevisiae* are indicated by light blue arrows. Domains were labeled in roman numerals.

494

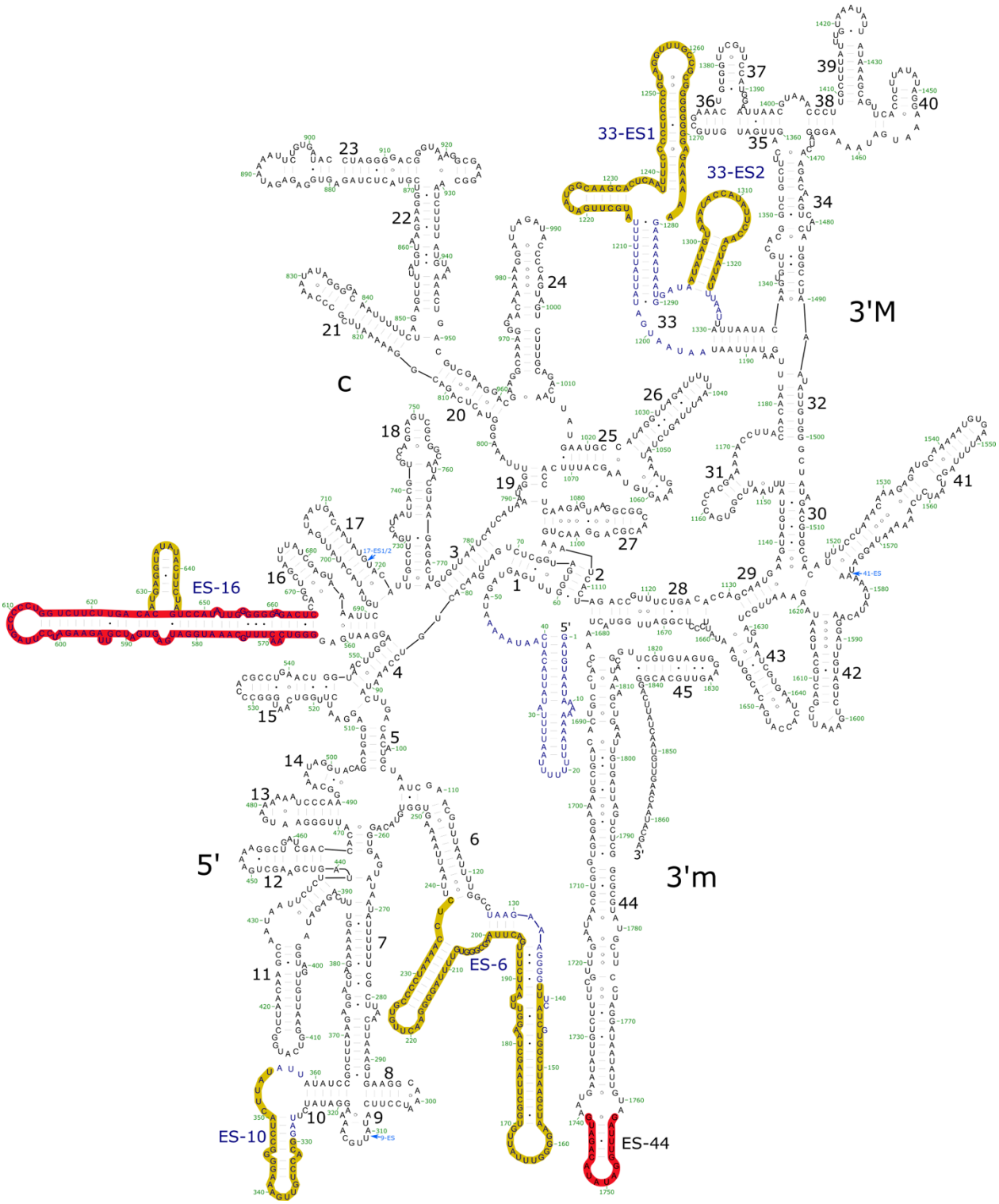

Figure S3B: Secondary structure diagram of the 16S rRNA of the mtSSU as estimated from the structure. The labeling is identical to Figure S2B.

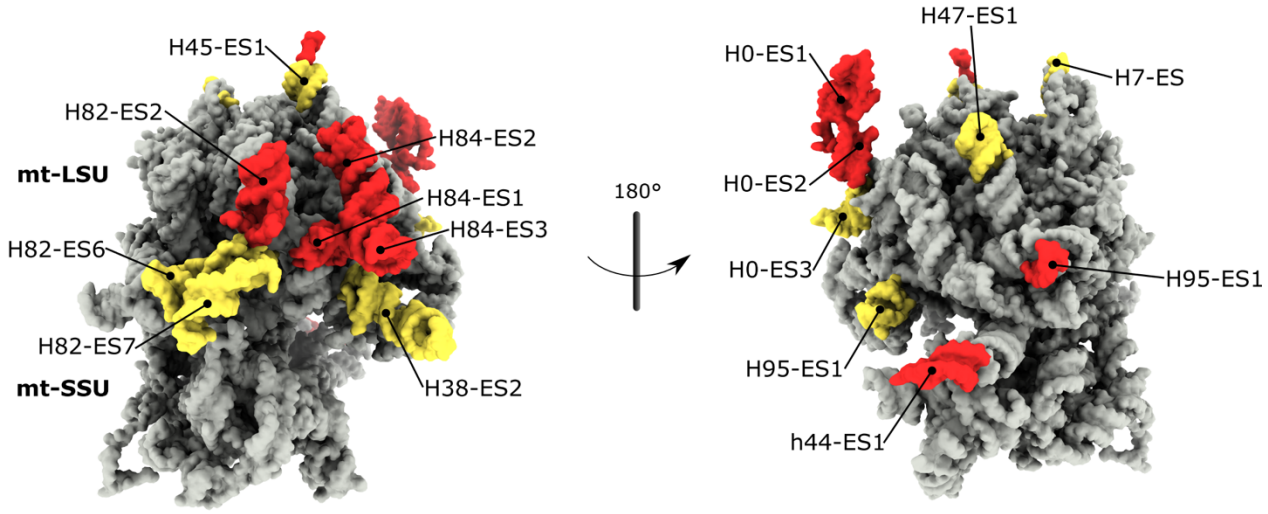

Figure S4: A three dimensional view of the rRNA of mtLSU and mtSSU of *N. crassa*. The rRNA conserved (bacteria) is shown in gray. ES shared with *S. cerevisiae* are shown in red and ES unique to *N. crassa* are shown in yellow.

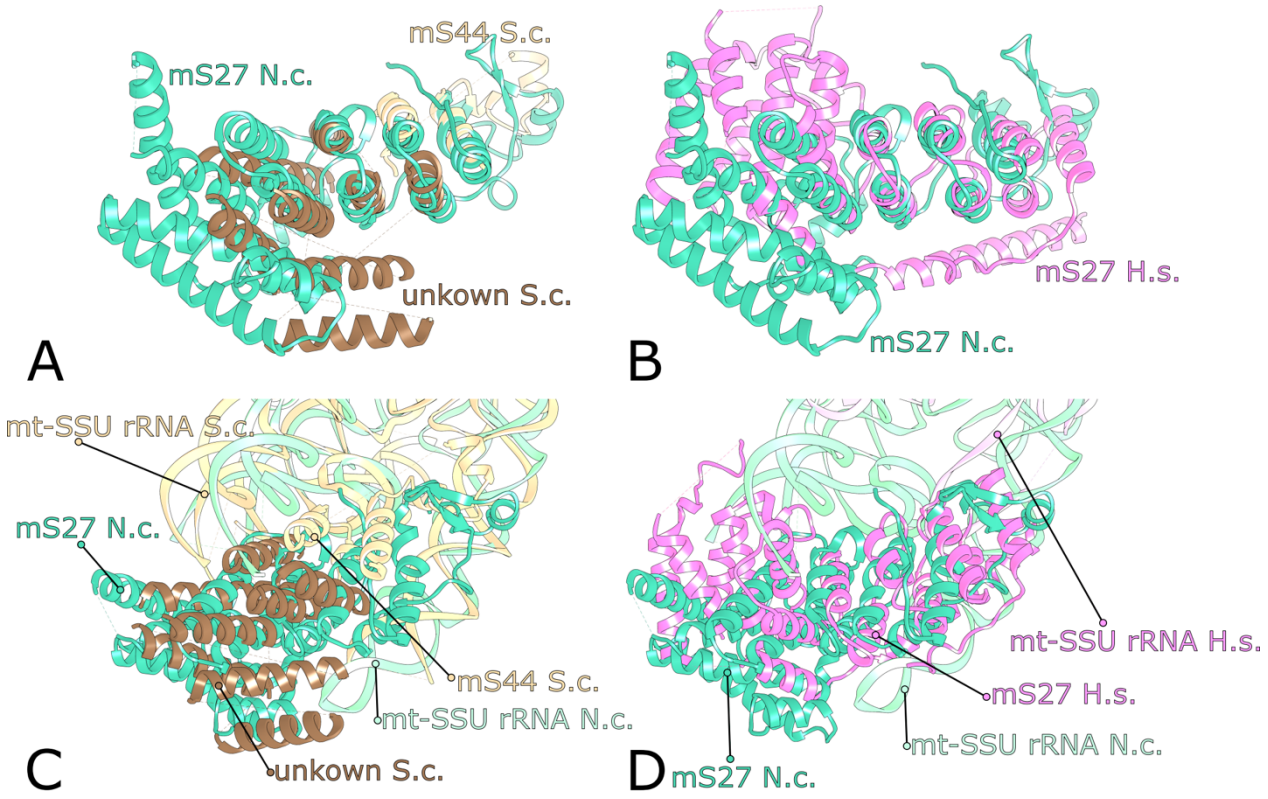

Figure S5: Superposition of different mS27 homologs. A: mS27 of *N. crassa* is superimposed with mS27 in *S. cerevisiae* (previously miss-assigned as mS44). **B:** Superposition of mS27 from *N. crassa* and human. **C:** Superposition based on mtSSU rRNA of mS27 from *N. crassa* and *S. cerevisiae* at the mtSSU tail. **D:** Superposition based on mtSSU rRNA of mS27 from *N. crassa* and *S. cerevisiae* at the mtSSU tail.

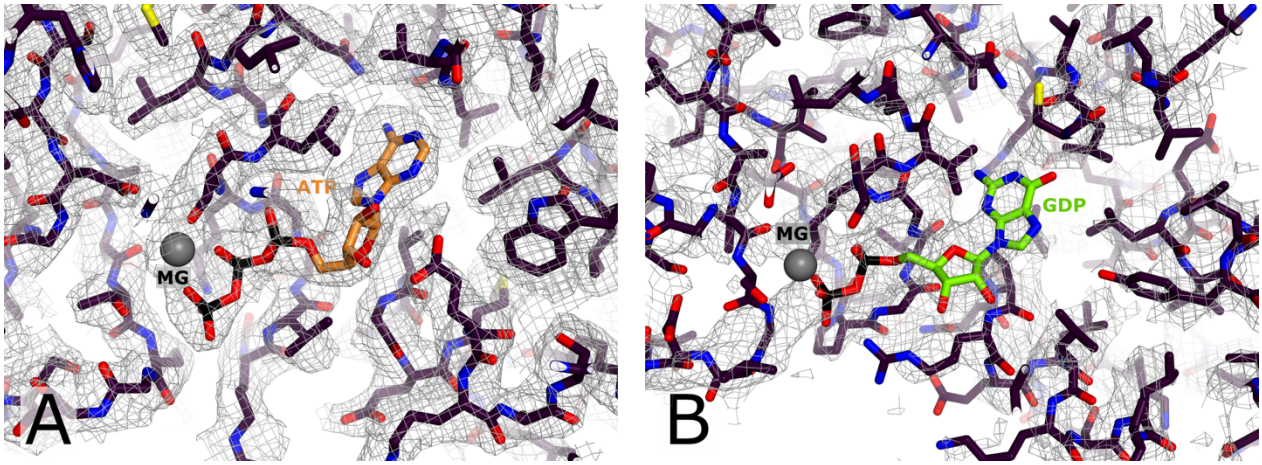

Figure S6: Comparison of the nucleotide binding pocket of mS29 between *N. crassa* and *S. cerevisiae* (PDB: 5mrc). A: The nucleotide pocket of *N. crassa* shown with density and ATP. **B:** Nucleotide pocket of *S. cerevisiae* shown with density and modeled GDP.

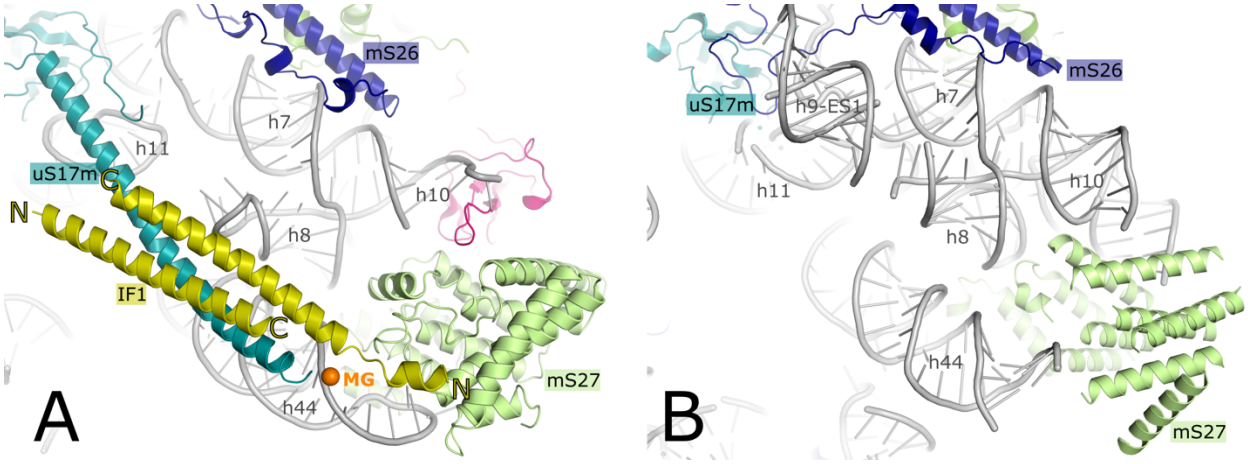

Figure S7: Side-by-side view of the mtSSU tail of *N. crassa and S. cerevisiae*. A: The binding site for IF_1 in *N. crassa*. B: The same site in *S. cerevisiae*.

522 **References**

523 Aibara S, Andréll J, Singh V, Amunts A (2018). "Rapid Isolation of the Mitoribosome from HEK
524 Cells." J Vis Exp **4**;(140).
525
526 Afonine, P. V., B. K. Poon, R. J. Read, O. V. Sobolev, T. C. Terwilliger, A. Urzhumtsev and P. D.
527 Adams (2018). "Real-space refinement in PHENIX for cryo-EM and crystallography." Acta
528 Crystallogr D Struct Biol **74**(Pt 6): 531-544.
529
530 Altschul, S. F., W. Gish, W. Miller, E. W. Myers and D. J. Lipman (1990). "Basic local alignment
531 search tool." J Mol Biol **215**(3): 403-410.
532
533 Amunts, A., A. Brown, X. C. Bai, J. L. Llacer, T. Hussain, P. Emsley, F. Long, G. Murshudov, S. H. W.
534 Scheres and V. Ramakrishnan (2014). "Structure of the yeast mitochondrial large ribosomal
535 subunit." Science **343**(6178): 1485-1489.
536
537 Amunts, A., A. Brown, J. Toots, S. H. W. Scheres and V. Ramakrishnan (2015). "Ribosome. The
538 structure of the human mitochondrial ribosome." Science **348**(6230): 95-98.
539 Baker, C. L., J. J. Loros and J. C. Dunlap (2012). "The circadian clock of Neurospora crassa." FEMS
540 Microbiol Rev **36**(1): 95-110.
541
542 Ban, N., R. Beckmann, J. H. Cate, J. D. Dinman, F. Dragon, S. R. Ellis, D. L. Lafontaine, L. Lindahl, A.
543 Liljas, J. M. Lipton, M. A. McAlear, P. B. Moore, H. F. Noller, J. Ortega, V. G. Panse, V.
544 Ramakrishnan, C. M. Spahn, T. A. Steitz, M. Tchorzewski, D. Tollervey, A. J. Warren, J. R.
545 Williamson, D. Wilson, A. Yonath and M. Yusupov (2014). "A new system for naming ribosomal
546 proteins." Curr Opin Struct Biol **24**: 165-169.
547
548 Beadle, G. W. and E. L. Tatum (1941). "Genetic Control of Biochemical Reactions in Neurospora."
549 Proc Natl Acad Sci U S A **27**(11): 499-506.
550
551 Brown, A., A. Amunts, X. C. Bai, Y. Sugimoto, P. C. Edwards, G. Murshudov, S. H. W. Scheres and
552 V. Ramakrishnan (2014). "Structure of the large ribosomal subunit from human mitochondria."
553 Science **346**(6210): 718-722.
554
555 Brown, A., S. Rathore, D. Kimanius, S. Aibara, X. C. Bai, J. Rorbach, A. Amunts and V.
556 Ramakrishnan (2017). "Structures of the human mitochondrial ribosome in native states of
557 assembly." Nat Struct Mol Biol **24**(10): 866-869.
558
559 David D. Perkins, Merle Glassey, and , Barbara A. Bloom (1962). "New data on markers and
560 rearrangements in Neurospora." Can J Genet Cytol. **4**: 187–205.
561
562 de Goede, P., J. Wefers, E. C. Brombacher, P. Schrauwen and A. Kalsbeek (2018). "Circadian
563 rhythms in mitochondrial respiration." J Mol Endocrinol **60**(3): R115-R130.
564

565 De Silva, D., Y. T. Tu, A. Amunts, F. Fontanesi and A. Barrientos (2015). "Mitochondrial ribosome
566 assembly in health and disease." Cell Cycle **14**(14): 2226-2250.
567
568 DeLano, W. L. (2002). "Pymol: An open-source molecular graphics tool. ." CCP4 Newsletter On
569 Protein Crystallography **40**: 82-92.
570
571 Desai, N., A. Brown, A. Amunts and V. Ramakrishnan (2017). "The structure of the yeast
572 mitochondrial ribosome." Science **355**(6324): 528-531.
573
574 Emsley, P. and K. Cowtan (2004). "Coot: model-building tools for molecular graphics." Acta
575 Crystallogr D Biol Crystallogr **60**(Pt 12 Pt 1): 2126-2132.
576
577 Esparza-Molto, P. B., C. Nuevo-Tapioles and J. M. Cuezva (2017). "Regulation of the H(+)-ATP
578 synthase by IF1: a role in mitohormesis." Cell Mol Life Sci **74**(12): 2151-2166.
579
580 Funes, S., F. E. Nargang, W. Neupert and J. M. Herrmann (2004). "The Oxa2 protein of
581 Neurospora crassa plays a critical role in the biogenesis of cytochrome oxidase and defines a
582 ubiquitous subbranch of the Oxa1/YidC/Alb3 protein family." Mol Biol Cell **15**(4): 1853-1861.
583
584 Galagan, J. E., S. E. Calvo, K. A. Borkovich, E. U. Selker, N. D. Read, D. Jaffe, W. FitzHugh, L. J. Ma,
585 S. Smirnov, S. Purcell, B. Rehman, T. Elkins, R. Engels, S. Wang, C. B. Nielsen, J. Butler, M.
586 Endrizzi, D. Qui, P. Ianakiev, D. Bell-Pedersen, M. A. Nelson, M. Werner-Washburne, C. P.
587 Selitrennikoff, J. A. Kinsey, E. L. Braun, A. Zelter, U. Schulte, G. O. Kothe, G. Jedd, W. Mewes, C.
588 Staben, E. Marcotte, D. Greenberg, A. Roy, K. Foley, J. Naylor, N. Stange-Thomann, R. Barrett, S.
589 Gnerre, M. Kamal, M. Kamvysselis, E. Mauceli, C. Bielke, S. Rudd, D. Frishman, S. Krystofova, C.
590 Rasmussen, R. L. Metzenberg, D. D. Perkins, S. Kroken, C. Cogoni, G. Macino, D. Catcheside, W.
591 Li, R. J. Pratt, S. A. Osmani, C. P. DeSouza, L. Glass, M. J. Orbach, J. A. Berglund, R. Voelker, O.
592 Yarden, M. Plamann, S. Seiler, J. Dunlap, A. Radford, R. Aramayo, D. O. Natvig, L. A. Alex, G.
593 Mannhaupt, D. J. Ebbole, M. Freitag, I. Paulsen, M. S. Sachs, E. S. Lander, C. Nusbaum and B.
594 Birren (2003). "The genome sequence of the filamentous fungus Neurospora crassa." Nature
595 **422**(6934): 859-868.
596
597 Goddard, T. D., C. C. Huang, E. C. Meng, E. F. Pettersen, G. S. Couch, J. H. Morris and T. E. Ferrin
598 (2018). "UCSF ChimeraX: Meeting modern challenges in visualization and analysis." Protein Sci
599 **27**(1): 14-25.
600 Greber, B. J., P. Bieri, M. Leibundgut, A. Leitner, R. Aebersold, D. Boehringer and N. Ban (2015).
601 "Ribosome. The complete structure of the 55S mammalian mitochondrial ribosome." Science
602 **348**(6232): 303-308.
603
604 Greber, B. J., D. Boehringer, A. Leitner, P. Bieri, F. Voigts-Hoffmann, J. P. Erzberger, M.
605 Leibundgut, R. Aebersold and N. Ban (2014). "Architecture of the large subunit of the
606 mammalian mitochondrial ribosome." Nature **505**(7484): 515-519.
607

608 Kaushal, P. S., M. R. Sharma and R. K. Agrawal (2015). "The 55S mammalian mitochondrial
609 ribosome and its tRNA-exit region." Biochimie **114**: 119-126.
610
611 Kim, H. J., P. Maiti and A. Barrientos (2017). "Mitochondrial ribosomes in cancer." Semin Cancer
612 Biol **47**: 67-81.
613
614 Kimanius, D., B. O. Forsberg, S. H. Scheres and E. Lindahl (2016). "Accelerated cryo-EM structure
615 determination with parallelisation using GPUs in RELION-2." Elife **5**.
616
617 Komoda, T., N. S. Sato, S. S. Phelps, N. Namba, S. Joseph and T. Suzuki (2006). "The A-site finger
618 in 23 S rRNA acts as a functional attenuator for translocation." J Biol Chem **281**(43): 32303-
619 32309.
620
621 Kuntzel, H. (1969). "Mitochondrial and cytoplasmic ribosomes from Neurospora crassa:
622 characterization of their subunits." J Mol Biol **40**(2): 315-320.
623
624 Kuntzel, H. and H. Noll (1967). "Mitochondrial and cytoplasmic polysomes from Neurospora
625 crassa." Nature **215**(5108): 1340-1345.
626
627 Li, X., P. Mooney, S. Zheng, C. R. Booth, M. B. Braunfeld, S. Gubbens, D. A. Agard and Y. Cheng
628 (2013). "Electron counting and beam-induced motion correction enable near-atomic-resolution
629 single-particle cryo-EM." Nat Methods **10**(6): 584-590.
630
631 Liebschner, D., P. V. Afonine, M. L. Baker, G. Bunkoczi, V. B. Chen, T. I. Croll, B. Hintze, L. W.
632 Hung, S. Jain, A. J. McCoy, N. W. Moriarty, R. D. Oeffner, B. K. Poon, M. G. Prisant, R. J. Read, J. S.
633 Richardson, D. C. Richardson, M. D. Sammito, O. V. Sobolev, D. H. Stockwell, T. C. Terwilliger, A.
634 G. Urzhumtsev, L. L. Videau, C. J. Williams and P. D. Adams (2019). "Macromolecular structure
635 determination using X-rays, neutrons and electrons: recent developments in Phenix." Acta
636 Crystallogr D Struct Biol **75**(Pt 10): 861-877.
637
638 McCluskey, K. and S. E. Baker (2017). "Diverse data supports the transition of filamentous fungal
639 model organisms into the post-genomics era." Mycology **8**(2): 67-83.
640
641 Nargang, F. E., M. Preuss, W. Neupert and J. M. Herrmann (2002). "The Oxa1 protein forms a
642 homooligomeric complex and is an essential part of the mitochondrial export translocase in
643 Neurospora crassa." J Biol Chem **277**(15): 12846-12853.
644
645 Neupert W, Sebald W, Schwab AJ, Massinger P, Bücher T (1969). " Incorporation in vivo of 14C-
646 labelled amino acids into the proteins of mitochondrial ribosomes from Neurospora crassa
647 sensitive to cycloheximide and insensitive to Chloramphenicol." Eur J Biochem **10**(3):589-91.
648
649 Ott, M., A. Amunts and A. Brown (2016). "Organization and Regulation of Mitochondrial Protein
650 Synthesis." Annu Rev Biochem **85**: 77-101.
651

652 Perkins DD, Radford A Sachs MS. (2001). "information on individual loci." San Diego, CA:
653 Academic press.
654
655 Petrov, A. S., E. C. Wood, C. R. Bernier, A. M. Norris, A. Brown and A. Amunts (2019). "Structural
656 Patching Fosters Divergence of Mitochondrial Ribosomes." Mol Biol Evol **36**(2): 207-219.
657
658 Pettersen, E. F., T. D. Goddard, C. C. Huang, G. S. Couch, D. M. Greenblatt, E. C. Meng and T. E.
659 Ferrin (2004). "UCSF Chimera--a visualization system for exploratory research and analysis." J
660 Comput Chem **25**(13): 1605-1612.
661 Sehnal, D., R. Svobodova Varekova, K. Berka, L. Pravda, V. Navratilova, P. Banas, C. M. Ionescu,
662 M. Otyepka and J. Koca (2013). "MOLE 2.0: advanced approach for analysis of
663 biomacromolecular channels." J Cheminform **5**(1): 39.
664 van der Sluis, E. O., H. Bauerschmitt, T. Becker, T. Mielke, J. Frauenfeld, O. Berninghausen, W.
665 Neupert, J. M. Herrmann and R. Beckmann (2015). "Parallel Structural Evolution of
666 Mitochondrial Ribosomes and OXPHOS Complexes." Genome Biol Evol **7**(5): 1235-1251.
667 Vogel, H. J. (1956). "A Convenient Growth Medium for Neurospora crassa." Microbial Genet.
668 Bull. **13**: 42-43.
669
670 van der Sluis EO, Bauerschmitt H, Becker T, Mielke T, Frauenfeld J, Berninghausen O, Neupert W,
671 Herrmann JM, Beckmann R (2015). "Parallel Structural Evolution of Mitochondrial Ribosomes
672 and OXPHOS Complexes." Genome Biol Evol **7**(5):1235-51.
673
674 Waterhouse, A., M. Bertoni, S. Bienert, G. Studer, G. Tauriello, R. Gumienny, F. T. Heer, T. A. P.
675 de Beer, C. Rempfer, L. Bordoli, R. Lepore and T. Schwede (2018). "SWISS-MODEL: homology
676 modelling of protein structures and complexes." Nucleic Acids Res **46**(W1): W296-W303.
677 Williams, C. J., J. J. Headd, N. W. Moriarty, M. G. Prisant, L. L. Videau, L. N. Deis, V. Verma, D. A.
678 Keedy, B. J. Hintze, V. B. Chen, S. Jain, S. M. Lewis, W. B. Arendall, 3rd, J. Snoeyink, P. D. Adams,
679 S. C. Lovell, J. S. Richardson and D. C. Richardson (2018). "MolProbity: More and better
680 reference data for improved all-atom structure validation." Protein Sci **27**(1): 293-315.
681 Woellhaf, M. W., F. Sommer, M. Schroda and J. M. Herrmann (2016). "Proteomic profiling of the
682 mitochondrial ribosome identifies Atp25 as a composite mitochondrial precursor protein." Mol
683 Biol Cell **27**(20): 3031-3039.
684
685 Zeng, X., M. H. Barros, T. Shulman and A. Tzagoloff (2008). "ATP25, a new nuclear gene of
686 Saccharomyces cerevisiae required for expression and assembly of the Atp9p subunit of
687 mitochondrial ATPase." Mol Biol Cell **19**(4): 1366-1377.
688
689 Zhang, K. (2016). "Gctf: Real-time CTF determination and correction." J Struct Biol **193**(1): 1-12.
690 Zheng, S. Q., E. Palovcak, J. P. Armache, K. A. Verba, Y. Cheng and D. A. Agard (2017).
691 "MotionCor2: anisotropic correction of beam-induced motion for improved cryo-electron
692 microscopy." Nat Methods **14**(4): 331-332.
693

Zivanov, J., T. Nakane, B. O. Forsberg, D. Kimanius, W. J. Hagen, E. Lindahl and S. H. Scheres (2018). "New tools for automated high-resolution cryo-EM structure determination in RELION-3." Elife **7**.

Zivanov, J., T. Nakane and S. H. W. Scheres (2019). "A Bayesian approach to beam-induced motion correction in cryo-EM single-particle analysis." IUCrJ **6**(Pt 1): 5-17.